

# Liquid Drawdown: Scalability Over Several Geometries

by

Fatemeh Safari-alamuti

A thesis submitted in partial fulfillment of the requirements for the degree of

Master of Science

in

Chemical Engineering

Department of Chemical and Materials Engineering

University of Alberta

© Fatemeh Safari-alamuti, 2018

## Abstract

This work examined liquid/liquid drawdown. Two tank geometries (ST and CIST) and three sets of impellers (PBT, A310, RT) were used. Water and Canola oil were the continuous and dispersed phases, respectively, with a holdup of oil of either 10% or 30%. First, the point of initial disruption of the interface ( $N_{id}$ ) and the point where the complete drawdown of oil into water occurred ( $N_{cd}$ ) were determined. Then the time ( $t_{cd}$ ) required to completely disperse the surface layer at  $N_{cd}$  and the power consumed ( $P$ ) were measured, from which the mixing energy ( $J_{cd}=P \cdot t_{cd}$ ) was calculated. In a second set of experiments, focused beam reflectance measurement (FBRM) was used to measure the transient chord length distribution (CLD) at  $N_{cd}$  and equilibrium time ( $t_{eq}$ ) and the transient Sauter mean chord length ( $cl_{32}$ ) were determined. Scaling results showed that the  $cl_{32}$  at  $t_{cd}$  scaled well with  $J_{cd}/m$ . Data also showed that the energy/ $cl_{32}$  correlation was independent of geometry and holdup when all impellers started the run in the continuous phase. Unlike energy, power per mass showed no clear trend with Sauter mean chord length. In addition,  $N_{cd}$  and  $t_{cd}$  were not scalable with power per mass. The results suggest that mixing energy is a useful scaling variable across several geometries. Comparison of  $cl_{32}$  with the Kolmogorov scale ( $\eta$ ) showed that the area weighted CLD falls above the Kolmogorov scale, while half of number weighted CLD is smaller than  $\eta$ . This observation is supported by recent studies of drop break-up based on tip streaming and a renewed interest in satellite drops.

## **Preface**

The first part of the work was performed by Akshay Bhalerao. That includes the measurement of the point at which the first drop of the oil entered the water phase ( $N_{id}$ ), the point of complete drawdown including the minimum rotational speed ( $N_{cd}$ ), and the time required to completely drawdown the oil phase ( $t_{cd}$ ).

## **Acknowledgment**

I would like to express my sincere gratitude to my supervisors, Dr. Kresta and Dr. Komrakova for their support and invaluable advice throughout my study at the University of Alberta.

I will also take this opportunity to express my thanks to my lab mates for their support and kindness Marcio Machado, Nitin Arora, Akshay Bhalerao, Khilesh Jairamdas, Colin Saraka, Dustyn Ulrich, Francesco Maluta and Anna Xu.

Finally, my heartiest gratitude is due to my dear husband, Hamed for his encouragement, help, support, and understanding throughout my study and research.

# Table of Content

Abstract .....	ii
Preface .....	iii
Acknowledgment .....	iv
List of Tables.....	vi
List of Figures .....	vii
List of Symbols .....	ix
1 Introduction .....	1
1.1 Drawdown of Dispersed Phase: Minimum Rotational Speed.....	3
1.2 CIST vs. Stirred Tank.....	4
1.3 Effect of Impeller Location and Phase Inversion.....	6
1.4 Mean Drop Size and Drop Size Distribution .....	8
1.5 FBRM and Chord Length Distribution .....	9
1.6 Effect of Dispersed Phase Holdup on Drop Size .....	11
1.7 Effect of Surfactant and Surface Charge.....	13
1.8 Equilibrium Time .....	13
1.9 Research Objectives .....	15
2 Experimental.....	18
2.1 Liquids and Geometries .....	18
2.2 $N_{id}$ and $N_{cd}$ Measurements .....	21
2.3 Transient Chord Length Distribution Measurement .....	22
2.4 Impeller Feed Experiments .....	23
3 Results and Discussion .....	26
4 Conclusion.....	58
5 Future Work.....	60
References .....	63
Appendix A: Conversion of Chord Length Distribution to Drop Size Distribution .....	69
Review of Available Methods.....	69
Method proposed by Hukkanen and Braatz (2003) .....	71
Coding and Numerical Results.....	73

## List of Tables

Table 1- Liquid Properties .....	19
Table 2- Dimensions of the stirred tank (ST) and confined impeller stirred tank (CIST).....	20
Table 3- Initial drawdown speed ( $N_{id}$ ), complete drawdown speed ( $N_{cd}$ ) and drawdown time ( $t_{cd}$ ) for CIST and ST .....	27
Table 4- Energy consumed for the complete drawdown normalized to the ST-RT-10.....	30
Table 5- Equilibrium time (max of $t_{eq-1}$ and $t_{eq-2}$ ) for surface layer and impeller feed experiments .....	40
Table 6- Equilibrium Sauter mean chord length ( $cl_{32-eq}$ ) and Sauter mean at the point of complete drawdown ( $cl_{32-cd}$ ) for Surface layer and at the end of feeding for Impeller feed experiments ....	49
Table 7- Comparison of chord length and Kolmogorov scale .....	52
Table 8- Power consumed, equilibrium and complete drawdown energy per mass for Surface Layer and Impeller Feed experiments.....	57

## List of Figures

Figure 1-Schematic image of (left) CIST and (right) ST. The volume of ST is equal to 10 L.....	5
Figure 2-FBRM probe and Chord Length Distribution histogram (Original picture from Mettler Toledo- Adapted with permission) .....	10
Figure 3- (left) (a)10% and (b) 30% hold up in the ST, (right) (c)10% and (d) 30% hold up in the CIST. The top impeller is immersed in the oil layer in the CIST-30% case. ....	20
Figure 4- (a) Point of interface disruption- $N_{id}$ , (b) complete drawdown speed- $N_{cd}$ .....	21
Figure 5- FBRM probe position in 10% holdup “Surface Layer” experiment: (a) CIST, probe located between second and third impeller with $45^\circ$ angle (b) ST, probe placed from top at the impeller level with $45^\circ$ angle.....	23
Figure 6- Feed pipe experimental setup. (a) Schematic drawing of CIST with FBRM port and feed pipe. (b) Close up of the feed pipe at the first impeller. (c) Image of feed pipe and the top impeller. The center of the pipe was at $r/R=0.85$ and the length of the feed pipe was 3.5 cm. ....	24
Figure 7- $N_{cd}$ vs. measured power per mass (P/m), (a) log-log plot (b) normal plot.....	29
Figure 8- (a) Number (b) Square weighted and (c) Cumulative chord length distribution (number weighted on left vertical axis and square weighted on right) for CIST-PBT DU-30 at the beginning of mixing process (from $t=0$ ) .....	34
Figure 9- (a) Number (b) Square weighted and (c) Cumulative chord length distribution for CIST-PBT DU-30 after equilibrium .....	38
Figure 10- Transient Sauter mean ( $cl_{32}$ ) for surface layer at $\phi=10\%$ and $30\%$ in ST. Dotted lines are equal to the equilibrium $cl_{32}$ . The filled and empty circles are $t_{cd}$ and $t_{eq}$ respectively .....	42
Figure 11- Transient Sauter mean ( $cl_{32}$ ) for surface layer at $\phi=10\%$ in CIST. The first and second dots are $t_{cd}$ and $t_{eq}$ .....	43
Figure 12- Transient Sauter mean ( $cl_{32}$ ) for impeller feed at $\phi=10\%$ in CIST. The filled and open dots are $t_{feed}$ and $t_{eq}$ . ....	44
Figure 13- Transient Sauter mean chord length ( $cl_{32}$ ) for impeller feed and surface layer in CIST (a) UD-10, (b) RT-10 and equilibrium chord length distribution of impeller feed and surface layer in CIST (c) UD-10, (d) RT-10.....	46
Figure 14- Transient Sauter mean ( $cl_{32}$ ) for surface layer at $\phi=30\%$ in CIST. The first and second dots are $t_{cd}$ and $t_{eq}$ .....	47
Figure 15-Sample Kolmogorov length on the CLD spectrum.....	51

Figure 16- Sauter mean chord length at the point of complete drawdown ( $cl_{32-cd}$ ) vs. Power per mass in log-log scale. 3 impellers (RT, PBT and A310) and two tank geometries (ST and CIST) were used. Configurations that the impeller is in the oil phase (CIST-30%) exhibit different slope than others ..... 54

Figure 17- Sauter mean chord length at the point of complete drawdown ( $cl_{32-cd}$ ) vs.  $J_{cd}/m$  in log-log scale. 3 impellers (RT, PBT and A310) and two tank geometries (ST and CIST) were used. Configurations that the impeller is in the oil phase (CIST-30%) exhibit different slope than others..... 55

Figure 18- Sauter mean chord length at the point of complete drawdown ( $cl_{32-eq}$ ) vs. complete drawdown energy grouped based on the impeller type. PBT-DD includes CIST-10, CIST-30, IF-10, ST-10 and ST-30. Fitted lines have similar slopes to Figure 16..... 56

Figure A-1-Cumulative log-normal drop size distribution vs. Calculated drop size distribution from matrix inversion ..... 75

Figure A-2-Experimental Chord Length Distribution measured by FBRM..... 76

Figure A-3-Drop size distribution calculated from experimental chord length distribution using direct matrix inversion ..... 76

Figure A-4-Cumulative drop volume distribution computed from experimental chord length distribution ..... 77

## List of Symbols

$A_{\text{imp}}$  = impeller area ( $\text{m}^2$ )

$A_{\text{pipe}}$  = feed pipe cross sectional area ( $\text{m}^2$ )

$C$  = impeller off-bottom clearance

$cl_{10}$  = number average chord length ( $\mu\text{m}$ )

$cl_{32}$  = Sauter chord length ( $\mu\text{m}$ )

$cl_i$  = nominal size of drops in class  $i$

$D$  = impeller diameter (m)

$d_{\text{pipe}}$  = pipe diameter (m)

$F$  = Taylor Number

$Fr$  = impeller Froude Number

$H$  = liquid height (m)

$J_{\text{cd}}$  = energy at complete dispersion point (J)

$J_{\text{eq}}$  = energy at equilibrium point (J)

$k$  = number of size classes that CLD is divided into

$l_e$  = turbulence macroscale (m)

$m$  = total mass of tank (kg)

$n_i$  = total number of drops

$N_{\text{jd1}}$  = impeller rotational speed at the point of interface disruption (rpm)

$N_{\text{jd2}}$  = impeller rotational speed at complete drawdown (rpm)

$N_Q$  = impeller flow number

$P$  = power (W)

$Q_{\text{feed}}$  = feed flowrate ( $\text{m}^3/\text{s}$ )

$Q_{\text{imp}}$  = impeller flowrate ( $\text{m}^3/\text{s}$ )

$r$  = distance from shaft (m)

$R$  = impeller diameter (m)

$T$  = tank diameter (m)

$t_{cd}$  = complete dispersion time (s)

$t_{eq}$  = equilibrium time (s)

$t_{inj}$  = impeller feed injection time (s)

$T_q$  = torque (N.m)

$V$  = tank volume ( $m^3$ )

$V_{oil}$  = total oil volume ( $m^3$ )

$We$  = Weber Number

### **Greek letters**

$\mu_c$  = water viscosity (Pa.s)

$\mu_d$  = oil viscosity (Pa.s)

$\nu$  = water kinematic viscosity ( $m^2/s$ )

$\rho_c$  = water density ( $kg/m^3$ )

$\rho_d$  = oil density ( $kg/m^3$ )

$\sigma$  = surface tension ( $J/m^2$ )

$\eta$  = Kolmogorov length scale ( $\mu m$ )

# 1 Introduction

Immiscible liquid/liquid systems are made up of at least two insoluble or partially immiscible liquids which separate into dispersed and continuous phases. A variety of industrial equipment is used to agitate immiscible liquids including stirred tanks, static mixers, extraction columns, and mixer-settlers. The stirred tank is commonly used to study mixing mechanisms and different aspects of liquid/liquid systems. The tank is equipped with an impeller, a shaft to connect the impeller to the motor, and baffles to recirculate the flow.

Liquid/liquid systems have extensive application in chemical, petroleum, food and pharmaceutical industries such as extraction, suspension polymerization, and multiphase reactions (Remacha et al. 2012; Maaß et al. 2010). Examples include the nitration of aromatic compounds (acid as a continuous phase and dispersed organic phase to be nitrated), separation of aqueous brine drops from crude oil to prevent corrosion, and control of drop size distribution (DSD) in emulsification and suspension polymerization (Paul et al. 2004). The main process objective in many of these systems is to maximize the contact between the liquid phases to enhance the available interfacial area for the mass transfer and chemical reaction (Becker et al. 2014).

Several aspects of liquid/liquid systems have been investigated by researchers. This includes energy dissipation inside the tank (Zhou & Kresta 1998b; You et al. 2014) effect of geometry (Zhou & Kresta 1998b; Giapos et al. 2005; Joshi et al. 2011), turbulence inside the tank (Baladyga & Podgórska 1998; Bałdyga et al. 2001), flow properties (Calabrese et al. 1986), CFD modelling of flow inside the tank (Alopaeus et al. 2002; Derksen & Van Den Akker 2007)(Podgórska & Marchisio 2016; T. Wang et al. 2013), measurement of dispersed phase drop size (Kraume 2012; Pandey et al. 2013; Mostafavi et al. 2016), and the effect of geometrical and physical properties

of the system on the drop size distribution (Remacha et al. 2012; Rueger & Calabrese 2013; Maaß et al. 2010).

Despite all of this work, liquid/liquid systems are still among the complex and least understood systems. This is because system properties are controlled by several interacting phenomena (Laurenzi et al. 2009). These phenomena include complex and scale dependent coalescence and breakup (Paul, E. L et al. 2004), possible phase inversion (Deshpande & Kumar 2003) and the effect of impurities (Leng & Calabrese 2004). Due to these complexities, liquid/liquid dispersion is still the subject of many active studies (Gao, Li, Buffo, Podgórska, et al. 2016; Becker et al. 2014; Rueger & Calabrese 2013a; Podgórska & Marchisio 2016; Afshar Ghotli et al. 2013; Cheng et al. 2015).

Drop breakup is a process of breakage of existing drops into at least two smaller drops. Drops break when the deforming forces (force induced by the surrounding fluid) exceeds the restoring force (surface and internal viscous forces) (Chesters 1991; Liao & Lucas 2009). Coalescence is the process of collision and combining of two or more drops into larger drops.

When the dispersed phase is added as the surface layer, the mixing proceeds in two steps, similar to floating solids in a solid-liquid system. The first step is the complete drawdown of the dispersed phase from the surface and the second step is the distribution of the dispersed phase throughout the tank, called dispersion (Khazam & Kresta 2008). The dynamics of both drawdown and dispersion play a significant role in determining system properties such as drop size distribution (Laurenzi et al. 2009). Thus, both drawdown and dispersion must be carefully studied. Drawdown is commonly characterized by the minimum rotational speed required to bring both liquids into contact throughout the entire mixing device. Dispersion is evaluated based on the distribution of drop size of the dispersed phase.

Although several studies have been reported in this field, there are still considerable interests in the study of drawdown and dispersion. One reason is the new developments in the industrial processes that changes the conventional methods, such as suspension polymerization that requires new studies on the mixing process (Maaß et al. 2010). Another reason is the advancement of the measurement techniques that enhances the experimental data acquisition in real time (Abidin et al. 2013). An example of advanced measurement technique is the focused beam reflectance measurement (FBRM) that provides in-situ drop size detection. FBRM measures the chord length as opposed to a diameter. Chord length is measured for any shapes of drops and particles.

In this chapter, we aim to review the summary of liquid/liquid dispersion and drawdown and parameters affecting drawdown. This review is followed by the summary of the recent work published in the area and list of research objectives of this project.

## **1.1 Drawdown of Dispersed Phase: Minimum Rotational Speed**

A primary process requirement in liquid/liquid dispersion is the complete drawdown of the less dense of the two phases. Therefore, identifying the minimum agitation speed to form a complete drawdown is of considerable importance (Armenante & Huang 1992). The rotational speed at which the interface is disrupted and the the first drop is drawn down is the point of interface disruption,  $N_{id}$ . The rotational speed at which the last pool of liquid is drawn down from the surface and the liquid is completely drawn down is  $N_{cd}$  and the time required to reach the point of complete drawdown is  $t_{cd}$ . There are similarities between  $N_{cd}$  and the minimum impeller speed for the complete suspension of solid in solid/liquid systems ( $N_{js}$ ) as both depend on density ratio and viscosity of continuous phase.  $N_{cd}$  also depends on interfacial tension.

Several studies have been published on the determination and prediction of  $N_{cd}$  and  $t_{cd}$  (Skelland & Lee 1978; Skelland & Ramsay 1987; Esch et al. 1971; Armenante & Huang 1992; Armenante

et al. 1992). In the majority of the literature, experiments have been performed to determine  $N_{cd}$  using a visual method.

Based on the results obtained from the experiments, several correlations have been proposed to predict  $N_{cd}$  from the impeller diameter, vessel dimensions, interfacial tension and the density difference (Armenante et al. 1992; Skelland & Ramsay 1987). The recommended correlation in the absence of experimental data is the one reported by Skelland & Seksaria (Skelland & Seksaria 1978). It includes the effect of tank and impeller geometry as well as the effect of physical properties of both phases on  $N_{cd}$ . In this equation,  $c$  and  $\alpha$  are system dependent constants and  $\Delta\rho$  is the density difference of dispersed and continuous phase (Skelland & Seksaria 1978).

$$\frac{N_{cd}D^{0.5}}{g^{0.5}} = c\left(\frac{T}{D}\right)^{\alpha}\left(\frac{\mu_c}{\mu_d}\right)^{1/9}\left(\frac{\Delta\rho}{\rho_c}\right)^{0.25}\left(\frac{\sigma}{D^2\rho_cg}\right)^{0.3} \quad (1)$$

Where,  $D$  is the impeller diameter,  $g$  is gravitational acceleration,  $T$  is the tank diameter,  $\mu_c$  and  $\mu_d$  are continuous phase and dispersed phase viscosity respectively,  $\Delta\rho$  is the density difference between two phases,  $\rho_c$  is the continuous phase density,  $\sigma$  is the interfacial tension and  $C, \sigma$  are system-dependent constants.

## 1.2 CIST vs. Stirred Tank

Two tank geometries are considered in this project: the conventional stirred tank (ST) and the confined impeller stirred tank (CIST). The CIST and ST schematics are shown in Figure 1.

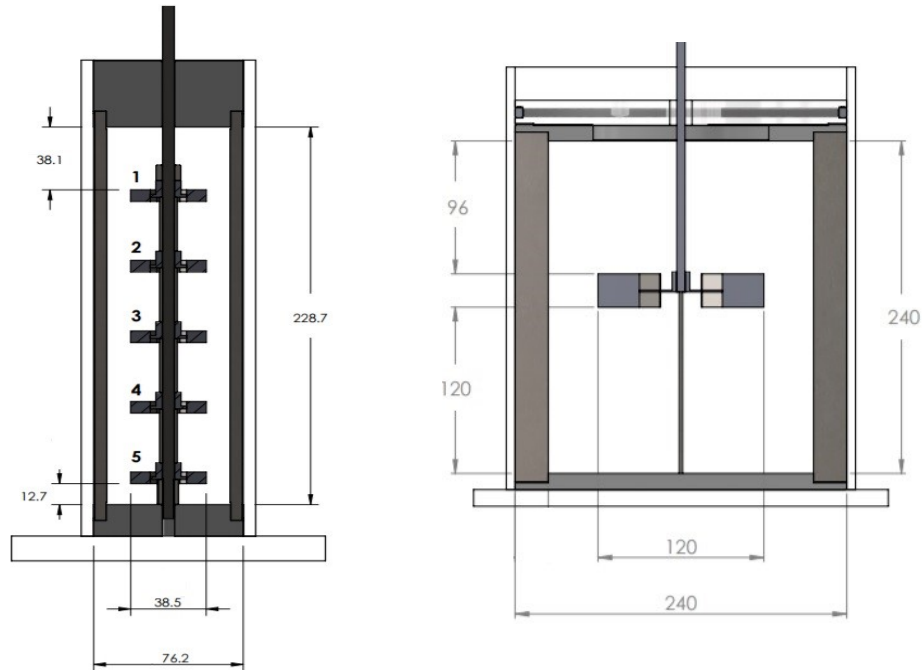


**Figure 1-Schematic image of (left) CIST and (right) ST. The volume of ST and CIST are 10L and 1L, respectively**

The conventional stirred tank is widely used to study mixing processes at the bench scale. The ST has liquid height equal to the tank diameter and is equipped with one impeller. It has been shown that in the ST, 30% of the tank does not participate in active circulation and mixing (Bittorf & Kresta 2000). Active circulation at the surface is important as chemical is often added at the surface. Moreover, the energy dissipation rate is not uniform and can vary by the factor of 100 in different locations inside the tank (Zhou & Kresta 1996).

Another important parameter when reproducing the mixing conditions of industrial scale process in bench scale is the Reynolds number which is defined as

$$Re = \frac{ND^2}{\nu_c} \quad (2)$$

Where, N is the impeller rotational speed, D is the impeller diameter and  $\nu_c$  is the continuous phase kinematic viscosity. The Reynolds number must be high enough to avoid transitional flow inside

the tank as transitional flow is not scalable. Machado et al showed that in the ST, a Reynolds number as high as  $3 \times 10^5$  is required to achieve fully turbulent flow in the entire tank (Machado et al. 2013). The large inactive volume (1/3 of the tank), inhomogeneous energy dissipation, and high Re requirements are significant problems of using ST to scale down the industrial mixing process. To resolve these issues, the confined impeller stirred tank was developed (Machado & Kresta 2013). The primary objective of the CIST was to enhance the uniform distribution of the energy dissipation inside the tank and to increase the active mixing volume (Machado & Kresta 2013). Results showed that fully turbulent flow throughout the CIST was achieved at Reynolds number 10 times less than a conventional stirred tank (Machado & Kresta 2013). CIST has a H/T ratio of 3 and is equipped with five impellers.

### **1.3 Effect of Impeller Location and Phase Inversion**

In liquid/liquid mixing, several factors define which phase to be a continuous phase. Several authors discussed that the initial location of the impeller has a significant effect on determining the continuous phase. It was shown that the phase in which the impeller was initially immersed became the continuous phase (Selkerl & Sleicher 1965; Treybal 1958; Quinn & Sigloh 1963; Yeo, L.Y.; Matar, O.K.; Perez de Ortiz, E.S.; Hewitt 2000). Kato et al. later showed this conclusion was not always true (Kato et al. 1991). They reported that which phase eventually becomes the continuous phase is a function of several parameters in addition to the initial impeller location such as oil volume fraction, impeller speed and height.

A related phenomenon to impeller location is the phase inversion. Phase inversion is a process of spontaneous interchange of continuous and dispersed phase such that dispersed phase becomes the continuous phase and vice versa. Phase inversion has extensive applications in food and

pharmaceutical industry and oil recovery (Perazzo et al. 2015) and is a complex process. This is because several parameters affect the phase inversion, including the impeller initial location, tank and impeller geometry, rotational speed, dispersed phase holdup, flow regime inside the tank and interfacial tension (Perazzo et al. 2015; Yeo et al. 2000).

Quinn and Sigloh (Quinn & Sigloh 1963) investigated the effect of the impeller rotational speed on the phase inversion of water/organic systems. They reported that for these system with equal volume fraction (1:1), the phase inversion occurred at the rotational speed equal to two to three times of the impeller speed when complete dispersion occurs. In a similar work, the effect of different factors including viscosity, density, rotational speed, dispersion formation method, shape and size of the vessel, impeller type and the material of the construction of the vessel was studied (Selkerl & Sleicher 1965). Their results showed that for any liquid/liquid system, in the wide range of volume ratio, either liquids could form a stable continuous phase. This range described as an ambivalent range was shown to be a function of the viscosity ratio of two phase. They also showed that the rotational speed had no effect on the ambivalent range when it was high enough to avoid settling/separation of the two phases. However, when the rotation speed was not high enough and some degree of settling/separation was observed, the ambivalent range decreased. The Authors also reported that density and interfacial tension had no effect on this range while the viscosity ratio showed a significant effect (Selkerl & Sleicher 1965). By increasing the viscosity ratio, the ambivalent range increased. Salager et al commented that the main factor defining the oil or water continuous phase was the local water to oil ratio at the initial impeller location (Salager et al. 2001). This water to oil ratio is different at different locations inside the tank and changes as the mixing proceeds.

## 1.4 Mean Drop Size and Drop Size Distribution

The size of dispersed phase drops inside the continuous phase is an important factor as it affects the emulsion stability and available interfacial area for diffusion, separation and chemical reaction (Paul et al. 2004). The drop size distribution in liquid/liquid systems is not uniform. Instead, it exists in a spectrum of the sizes, referred to as the drop size distribution (DSD). The DSD is usually represented in terms of a number weighted distribution,  $f_n(d_i)$ , or volume weighted distribution,  $f_v(d_i)$ . These parameters are given by Equation 3 and 4.

$$f_n(d_i) = \frac{n_i}{\sum_{j=1}^m n_j} \quad (3)$$

$$f_v(d_i) = \frac{n_i d_i^3}{\sum_{j=1}^m n_j d_j^3} \quad (4)$$

In these equations,  $n_i$  is number of drops,  $m$  is the number of bins,  $n_j$  is number of drops in  $j^{\text{th}}$  bin,  $d_i$  and  $d_j$  are the representative drop size of  $i^{\text{th}}$  and  $j^{\text{th}}$  bin, respectively

The DSD is also commonly reported as the cumulative distribution (Equation 5).

$$f_v(d_k) = \frac{\sum_{i=1}^k n_i d_i^3}{\sum_{j=1}^m n_j d_j^3} \quad (5)$$

The *Sauter mean diameter*,  $d_{32}$ , is commonly used to represent the mean drop size which relates the area of the dispersed phase to its volume, which is important for mass transfer applications.

(Equation 6)

$$d_{32} = \frac{\sum_{i=1}^m n_i d_i^3}{\sum_{i=1}^m n_i d_i^2} \quad (6)$$

In this equation,  $m$  is the number of size domains describing the DSD,  $n_i$  is the number of drops in each domain, and  $d_i$  the nominal diameter of drops in size class  $i$ .

Drop sizes depend on several factors such as tank and impeller geometry, impeller type, dispersed phase holdup, dispersed phase viscosity and viscosity ratio (ratio of dispersed to continuous phase), energy dissipation rate.

To measure transient drop size distribution, varieties of experimental techniques have been used (Abidin et al. 2013). These techniques are divided into two groups of in-situ that takes the measurement inside the tank and ex-situ that requires sample withdrawal from the vessel and post processing of the sample. In this work the focused beam reflectance measurement FBRM was used to measure the transient chord length distribution of the dispersed phase.

## 1.5 FBRM and Chord Length Distribution

Focused beam reflectance measurement (FBRM) is widely used in different industries such as food, chemical and petroleum (Ruf et al. 2000; Maaß et al. 2009; Boxall et al. 2012; Boxall et al. 2010). FBRM provides prompt, in-situ particle size analysis with limited post-processing requirements. Several researchers have used FBRM to measure DSD in o/w and w/o dispersions with different compositions and dispersed phase holdups (Boxall et al. 2010; Wang et al. 2013; Alopaeus et al. 2002; Cameirao et al. 2012; Ferreira & Trierweiler 2009). FBRM size detection ranges from  $2\mu\text{m}$  to  $2000\mu\text{m}$ .

The schematic illustration of FBRM measurement is presented in Figure 2. When the FBRM probe is immersed into the system, a scanning laser beam is focused to a fine spot close to the sapphire window interface and continuously scans a circle of approximately 8 mm diameter. The laser light is then backscattered to the detector inside the probe by individual particles. These backscattered light pulses are detected and translated into the value called the *chord length*. This calculation is

done by multiplying the scan speed (velocity) into the pulse width (time) and is the length of the straight line from one edge of a particle to another edge. Since the beam tangential velocity is known (2 m/s), pulse width is directly proportional to the intersected particle width but as it is not probable that laser beam exactly passes through particle diameter, intersected particle width is treated as the chord length. As there are several thousands of particles with different sizes, thousands of different chord lengths are measured each second and the chord length Distribution (CLD) is reported (Heath et al. 2002). The common time interval of the CLD measurement is 10 seconds. It is also possible to perform the measurements faster (e.g. 2 second and 5 second intervals).

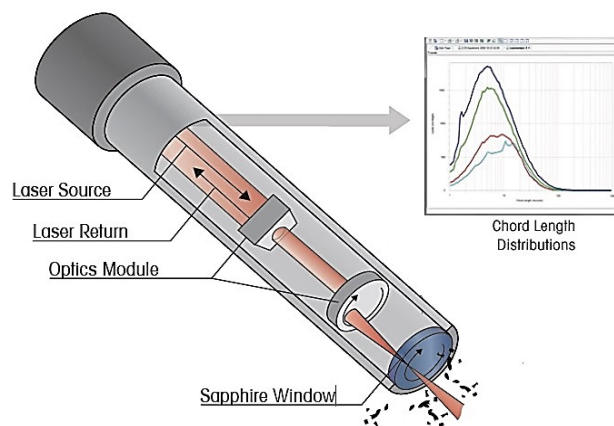


**Figure 2-FBRM probe and Chord Length Distribution histogram (Original picture from Mettler Toledo- Adapted with permission)**

It is recommended by Mettler Toledo that to obtain the optimum CLD measurements, the FBRM probe be placed in the main flow direction with the angle of 30-60°. This is to minimize the effect of stagnant drops to the sapphire window on the chord measurement.

As mentioned, the dispersed phase drop size inside the tank is polydisperse. The whole distribution is divided into the limited number of bins. Number and volume weighted distributions are two common representations of the drop size distribution (DSD). Similarly, CLD is reported in the form of number weighted distribution. However, as the chord length is not always equal to the drop diameter, the volume weighted distribution does not have a meaningful implication for CLD. Instead, a square weighted distribution is calculated and reported. To calculate square weighted distribution, first the bins are weighted. Each bin is defined by the chord length range ( $cl_i, cl_{i+1}$ ) and the total number of counts of that specific range ( $c_i$ ). The weighted count is then defined (Equation 7).

$$y_i = w_i c_i \quad (7)$$

In this equation,  $y_i$  is weighted count of  $i^{\text{th}}$  bin,  $c_i$  is the original number of count of  $i^{\text{th}}$  bin and  $w_i$  is the weighting factor defined by the equation recommended by Mettler Toledo (Equation 8).

$$w_i = \frac{M_i^\gamma}{\sum_{j=1}^N M_j^\gamma} N \quad (8)$$

$\gamma$  is the weighting factor,  $M_i$  is the midpoint chord length of  $i^{\text{th}}$  bin which is equal to the average of min and max chord length in that bin ( $M_i = \frac{cl_i + cl_{i+1}}{2}$ ) and  $N$  is the total number of bins. For the square weighted distribution,  $\gamma$  is equal to 2 and in the number weighted distribution  $\gamma$  is 1.

## 1.6 Effect of Dispersed Phase Holdup on Drop Size

The dispersed phase holdup is an important process parameter that affects the drop size. Effect of dispersed phase holdup on drop size distribution is investigated by several researchers (Boxall et al. 2010; Vankova et al. 2007; Becker et al. 2014). Three main interpretations have been used to

explain the effect of holdup: turbulence damping, coalescence and change of dispersion effective viscosity (Razzaghi & Shahraki 2010).

Maaß et al studied the effect of the dispersed phase hold up on drop size in low viscosity systems with hindered coalescence (Maaß et al. 2012). The mixing was studied in a stirred tank. The viscosity of the emulsion ranged between 0.47 to 1.15 mPa.s. Their analysis was focused on the drop breakage process. Their results showed a strong dependency of drop size on the holdup ranging from 2 to 45 vol%. The drop size increased with increasing the dispersed phase holdup, even with no coalescence. They measured the viscosity for different holdups and observed that the holdup had no effect on the viscosity. As the coalescence was hindered and viscosity showed no effect, they attributed the increase in the drop size to the turbulence hindering which affected the breakup process. They explained that by increasing the holdup the turbulence intensity was reduced, resulting in the decreased breakup rate which resulted in a larger average drop size. In all cases, the impeller was dispersed in the continuous phase.

Few reports were found that attempted to explain the effect of holdup from the change of the viscosity. Doulah explained the effect of holdup on drop size based on the dispersion viscosity (Doulah 1975). It was observed that change of the dispersed phase holdup changed the dispersion viscosity. This change of the viscosity altered the turbulence by changing the average length scale of the eddies, which affected the breakup mechanisms and changed the drop size.

Delichatsios & Probstein explained the effect of hold up by the coalescence (Delichatsios & Probstein 1976). They studied the liquid/liquid system with both breakup and coalescence and observed increases in the drop size by increasing the dispersed phase holdup which was attributed to the increase of the coalescence rate. By increasing the holdup, the number of drops increased

inside the tank which increased the probability of drop collision which resulted in the increase of coalescence rate and average drop size.

### **1.7 Effect of Surfactant and Surface Charge**

Surfactant is commonly used to stabilize the system against coalescence. The surfactant concentration, composition and functionality depend on the system being studied and on the process requirements. Surfactants affect the surface mobility by reducing the interfacial tension and hindering coalescence (Paul et al. 2004). Besides reducing the interfacial tension, surfactant changes the interfacial rheology and alters the drop deformation, drop breakup and coalescence significantly (Padron 2005). Even a small amount of surfactant or impurity can change the system behaviour dramatically. This is because the coalescence depends strongly on the interface rigidity and the electrical double layer around the drop (Maaß et al. 2012). By increasing the surfactant concentration, the interfacial tension decreases first, and then remains constant as the concentration reaches critical micellization value, CMC (Maaß et al. 2012).

The effect of surfactant (and interfacial tension) decreases as the dispersed phase viscosity increases (Wang, et al. 1986; Padron 2005). At high dispersed phase viscosity, or high viscosity ratio ( $\mu_d/\mu_c > 10$ ), interface deformation is controlled mainly by the viscous stress. It is also shown that at higher interfacial tension (lower concentration of surfactant), drop size distributions is broader due to the higher resistance to the breakage (Wang, et al. 1986).

### **1.8 Equilibrium Time**

The equilibrium time ( $t_{eq}$ ) is the time after which the chord length distribution and the mean drop size remain unchanged.  $t_{eq}$  is industrially important as it shows for how long the two phases should be agitated to obtain the desired drop size. Different studies show that  $t_{eq}$  depends on the mixing

condition and physical properties of two phases (Hong & Lee 1983a; Ceylan et al. 2003; Poblete et al. 2016). Hong and Lee reported that the time to reach the equilibrium drop size was much shorter for the system with both coalescence and breakup than with breakup only (Hong & Lee 1985). In the latter case, several hours might be required to reach the equilibrium drop size, as the breakup rate decreases considerably over time (Wang & Calabrese 1986). If mixing continues for long enough,  $d_{32}$  may increase slightly due to the slow coalescence rates becoming important as breakage rate decreases (Blount 1995).

The main method reported by the researchers to define  $t_{eq}$  is based on the visual technique (Chatzi, Costas J Boutris, et al. 1991; Hong & Lee 1983b). In this method, the transient drop size distribution or transient Sauter mean diameter is plotted versus time and the time DSD or  $d_{32}$  remained almost constant was noted as  $t_{eq}$ . This method is rough, system-dependent and requires to perform an experiment on each system.

Besides visual methods, Hong et al. (Hong & Lee 1985) suggested a correlation to predict the equilibrium time (Equation 9-11) based on the results obtained from 181 runs. This equation was used to calculate the  $t_{eq}$  for both impeller feed and surface layer setups. However, the calculated  $t_{eq}$  was much shorter than the one defined visually. It underestimated the required time to reach the dynamic steady-state point and could not predict the  $t_{eq}$  accurately. Thus, visual method remained the best technique to define the  $t_{eq}$ .

$$Nt_{eq} = 1995.3 * \left(\frac{D}{T}\right)^{-2.37} F^{0.97} \frac{\mu_d}{\mu_c} F_r^{-0.66} \quad (9)$$

$$F = \frac{We}{Re} \quad (10)$$

$$F_r = \frac{\rho_c D^2 N^2}{\Delta\rho H g} \quad (11)$$

In these equation,  $N$  is the rotational speed,  $D$  and  $T$  are impeller and tank diameter respectively,  $F$  is Taylor number,  $Fr$  is impeller Fraud number,  $\mu_d$  and  $\mu_c$  are dispersed phase and continuous phase viscosity respectively,  $\rho_c$  is the continuous phase density,  $\Delta\rho$  is the density difference of two phases,  $H$  is the liquid height and  $g$  is the gravity acceleration.

By reviewing the published literature in the field of liquid drawdown, we identified couple of research gaps and listed research objectives to address them to improve the understanding of the complex liquid/liquid system. Next part summarizes the research objectives and outlines the approach to address them

## **1.9 Research Objectives**

The first goal of this project was to explore the liquid drawdown from the surface in two geometries: the convectional stirred tank (ST) and the confined impeller stirred tank (CIST) that was designed to provide more uniform agitation and reproducible bench scale data (Machado & Kresta 2013). The performance of the two tanks was compared using a number of measures. Three types of impellers at two dispersed phase holdups (10%, 30%) were used. In the first phase of the project, the correlation of power per mass with the minimum speed required to completely disperse two phases ( $N_{cd}$ ) was investigated to explore the possibility of scaling the  $N_{cd}$  over several geometries.

The results obtained from the first phase of the project revealed that in ST increasing the holdup increased the energy required for the complete dispersion ( $J_{cd}$ ), while increasing the holdup in CIST, decreased  $J_{cd}$ . A possible explanation of this finding was that configurations with higher  $J_{cd}$ , results in smaller drop size. Evaluation of this hypothesis was the second goal of the project. To pursue this objective, a transient chord length distribution was measured for different geometries

using FBRM. An impeller feed experiments as opposed to a surface drawdown were also performed to determine its effect on the mixing properties of two phase, such as mixing energy and size of dispersed phase drops. The data obtained were used to investigate if it was possible to scale the results across several geometries.

The third objective of this work was to explore the correlation of the chord length with the operating parameters such as power and mixing energy was explored as a scaling parameter across several geometries. As mentioned, chord length is different from the drop size. As it does not include any assumption for the shape of the drop, it can be reported for both spherical and non-spherical drops. This is the first attempt reported so far to correlate the chord length with operating parameter. Most of the works published in the literature considered correlation of maximum and Sauter mean drop size with the drop Weber number ( $We$ ) (Hinze 1955; Maaß et al. 2012; Angle & Hamza 2006; Calabrese et al. 1986). Although very common, drop size- $We$  correlation has several limitations. The first one is that this correlation considers only effect of physical properties (viscosity, density, interfacial tension) and dispersed phase holdup on drop size. It ignores the effect of geometry and operating parameters on the drop size (Maaß et al. 2010). Another problem of this correlation is that it assumes a linear dependence of drop size on the holdup which is not supported by the experimental data (Kraume et al. 2004; Angle & Hamza 2006; Zhou & Kresta 1998a). Moreover, the correlation of Sauter mean drop size and Weber number is based on the assumption of linear relation of Sauter mean drop ( $d_{32}$ ) size and maximum drop size ( $d_{max}$ ) (Sprow 1967). However, it is shown that the linear correlation of  $d_{32} - d_{max}$  is questionable. It is only valid for a limited range of operating conditions (Zhou & Kresta 1998a).

Besides the study of the drawdown and scaling of chord length, a method to define an equilibrium time from transient chord length data was also provided in this research project. Equilibrium time

( $t_{eq}$ ) is a time after which the size and the distribution of the dispersed phase drops remains unchanged.

In the next chapter, first summary of the experimental work is presented followed by the results. In the experimental part, liquids used and geometries tested are reported. Then, the measurement techniques for the rotational speed at which the first drop of dispersed phase entered the continuous phase, ( $N_{id}$ ), the complete drawn-down speed ( $N_{cd}$ ) and drawdown time ( $t_{cd}$ ) is summarized. Next the measurement method to record the transient chord length distribution is summarized. Then, to explore the effect of the addition of dispersed phase to the continuous phase, the impeller feed experiment verses the surface layer setup is presented. Following the experimental section, the results obtained are discussed in five sections, including the effect of geometry, equilibrium time definition and results, transient Sauter mean chord length in CIST, ST, and effect of impeller feed vs. surface layer and finally scaling of  $cl_{32}$  with power and energy. The last section of the paper chapter is the conclusion. At the end, the thesis is wrapped up by the future work chapter, outlining the recommended works to further expand.

## 2 Experimental

In this study, drawdown and dispersion of oil into water was studied. The experimental work was done in three parts. First, the drawdown of a surface layer was examined across two tank geometries. The rotational speeds at the point where the interface is disrupted and the first drop is drawn down ( $N_{id}$ ) and where the last pool of liquid is drawn down from the surface and the liquid is completely drawn down ( $N_{cd}$ ) were recorded, as well as the torque at both speeds. Second, the experiment was repeated starting at  $N_{cd}$ , and the time required to completely drawdown the surface layer ( $t_{cd}$ ) was determined. During these experiments, the transient chord length distribution was also measured using focused beam reflectance measurement (FBRM). To determine the effect of feed position on the development of the drop size distribution (as represented by the chord length distribution), a third set experiments with feed at the impeller was performed for a sub-set of the geometries studied. In the impeller feed experiments, the dispersed phase was fed at the upper surface of the top impeller over a total feed time equal to 80% of  $t_{cd}$  and the transient chord length distribution and torque were recorded. The correlation of mean chord length to mixing power and mixing energy was tested across a number of experimental conditions.

### 2.1 Liquids and Geometries

The fluid properties are given in Table 1. In all experiments, Canola oil was dispersed into tap water. The volume fraction of Canola oil was either 10% or 30%.

**Table 1- Liquid Properties**

<b>Fluid Properties</b>	<b>Water</b>	<b>Canola Oil</b>
$\sigma$ (mN/m)	20.51 $\pm$ 0.58	
$\rho$ (kg/m <sup>3</sup> )	1000	914
$\mu$ (Pa.s)	10 <sup>-3</sup>	0.0715

A pendant drop apparatus was used to measure the interfacial tension between the water and oil. This method is based on the principle that the volume reached by a droplet of the one liquid into the other liquid is proportional to the interfacial tension between the two liquids and is given by the following equation (Paul et al. 2004):

$$\sigma = \frac{\theta V_d \Delta \rho g}{2\pi r} \quad (12)$$

where  $V_d$  : volume of detached drop,  $\Delta \rho$  : difference in densities of the two phases,  $g$ : acceleration due to gravity and  $r$ : radius of hypodermic needle. The Canola oil and water viscosity and density were taken from (Lang et al. 1992 and Azian et al. 2001).

The dimensions of the tanks are given in Table 2. Three types of impellers (A310, PBT and Rushton (RT)) and two tank geometries were used: a stirred tank (ST) with a single impeller and  $H=T$ ; and a confined impeller stirred tank (CIST) with 5 impellers and  $H=3T$ .

**Table 2- Dimensions of the stirred tank (ST) and confined impeller stirred tank (CIST).**

Specification	ST	CIST
Tank diameter (m)	0.24	0.076
Liquid height	T	3T
Impeller diameter	T/2	T/2
Impeller off-bottom clearance	T/2	D/3
Impeller submergence	S	D
Impeller blade height	D/5	D/4
Baffle width	T/10	T/12
Number of baffles	4	4

Figure 3 shows the two test vessels at 10% holdup and 30% holdup. The CIST was equipped with 5 evenly spaced impellers for each experiment. For the PBT, three different pumping configurations were tested: UDUDU, DUDUD and DDDDD (D= down-pumping, U= up-pumping). In the case of the ST, a single impeller at  $C=T/2$  was used and the PBT was always down-pumping.

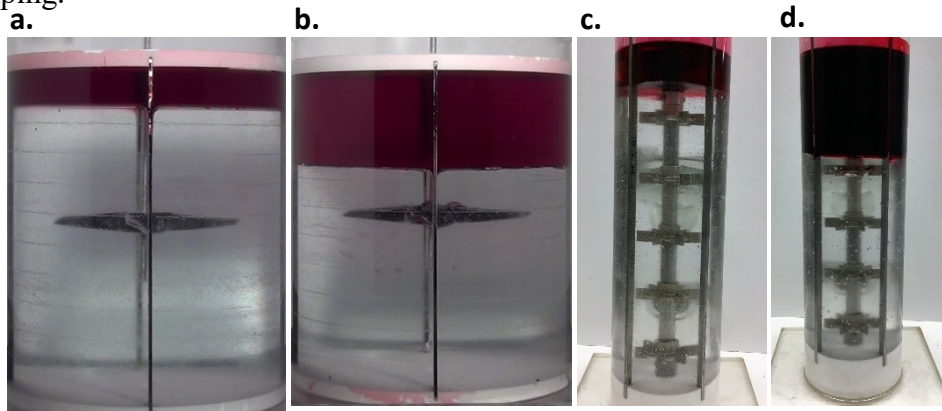


**Figure 3- (left) (a)10% and (b) 30% hold up in the ST, (right) (c)10% and (d) 30% hold up in the CIST. The top impeller is immersed in the oil layer in the CIST-30% case.**

## 2.2 $N_{id}$ and $N_{cd}$ Measurements

Figure 4 shows the point of interface disruption ( $N_{id}$ ) and the point of complete drawdown ( $N_{cd}$ ) in the ST.

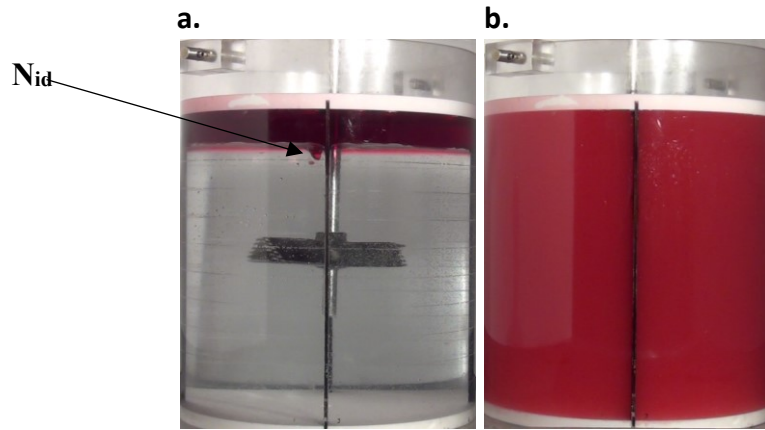


**Figure 4- (a) Point of interface disruption- $N_{id}$ , (b) complete drawdown speed- $N_{cd}$**

In total, 16 experiments were performed. Ten experiments were done in the CIST (5 impeller configurations at two holdups) and 6 experiments were done in the ST (3 impellers at two holdups). In all cases, the total volume displaced by the shaft and impellers was measured. For the ST, this volume was small (100 ml) compared to the total volume of the tank (10L). For the CIST, this volume was 2.5 % of the tank volume (25 ml). To determine the amounts of oil and water needed, a volume correction was applied. To improve the visibility of the oil, two to three drops of red-coloured Leak-Detecting Dye (Bright Dyes Solvent, Kingscote Chemicals Inc.) were added to the oil. The oil was slowly poured into the water to avoid mixing. Once the interface was stationary, the motor was turned on and the rotational speed of the impeller was increased gradually until the interface was disturbed and the first drop of oil was drawn down into the water. In this step, no fixed increment was applied and  $N_{id}$  was defined based on visual observation. This impeller rotational speed was recorded as  $N_{id}$ .

To determine  $N_{cd}$ , the liquid was observed for five minutes at each impeller speed. The CIST tests started at 50 rpm with initial increments of 50 rpm, later reduced to 25 rpm. For the ST, the initial increment was 10 rpm, later reduced to 5 rpm. The increment was smaller for the ST than the CIST because the changes were more abrupt in the ST, perhaps suggesting that the interface is disrupted at the point where the wall jet reaches the interface (Bittorf & Kresta 2001).

In order to determine the time required to achieve complete drawdown ( $t_{cd}$ ), each test was repeated at  $N_{cd}$ . The time required to completely drawdown the oil was recorded using a stopwatch.

There was no significant change in temperature over the course of any of these experiments.

### **2.3 Transient Chord Length Distribution Measurement**

An FBRM probe by Mettler-Toledo (Columbia, MD, USA; model: Particle Track G400) was used to measure the transient chord length distribution (CLD). The FBRM probe has a laser beam which continuously scans an 8mm diameter circle with a tangential velocity of 2 m/s. The laser light is backscattered to the detector and when the drop interface crosses the light beam, the scattering changes amplitude. The length of this high or low amplitude signal is translated into the chord length (Schümann et al. 2015). The chord length is the length of the straight line from one drop interface to the next and is calculated by multiplying the scan velocity by the pulse width (time). Figure 5 shows the probe positions for chord length measurements in both the CIST and ST at 10% holdup. As shown in Figure 5 in the CIST, the FBRM probe was inserted into the vessel through a side port between the second and third impellers at an angle of  $45^\circ$ . In the ST, the probe was inserted from the top at an angle of roughly  $45^\circ$  and placed at the impeller height close to the upstream of the baffle. For both vessels, the total volume of liquid displaced by the probe tip was negligible (0.5% of the tank volume). After the probe was inserted, water and oil were carefully added to develop a stable interface. Chord length data was collected from the onset of mixing ( $t=0$ )

for 100 min to ensure that the onset of equilibrium was captured. This normally occurred about 30 min after mixing began.

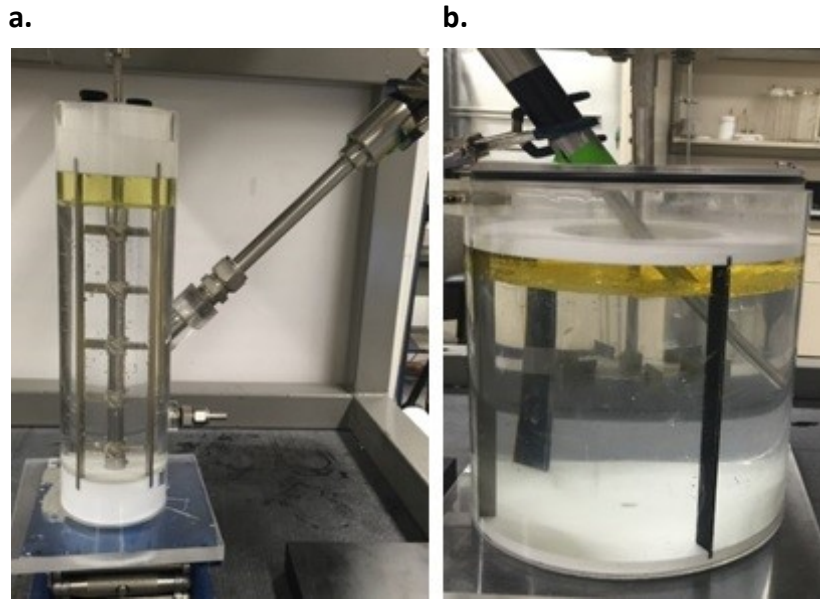


**Figure 5- FBRM probe position in 10% holdup “Surface Layer” experiment: (a) CIST, probe located between second and third impeller with 45° angle (b) ST, probe placed from top at the impeller level with 45° angle**

## 2.4 Impeller Feed Experiments

Figure 6 shows the impeller feed experimental setup. In this set of experiments, the dispersed phase was fed at the upper surface of the top impeller over a total feed time equal to 80% of  $t_{cd}$ . The feed pipe used to inject the dispersed phase had an inside diameter of 0.6 cm and height of 3.5 cm. The centre of the pipe was placed at  $r/R=0.85$ .

The feed pipe diameter was specified so that the feed velocity did not exceed the impeller discharge velocity. The feed flowrate was specified based on the injection time ( $0.8t_{cd}$ ) and oil holdup.

$$t_{inj} = 0.8t_{cd} \quad (13)$$

$$Q_{\text{feed}} = \frac{V_{\text{oil}}}{t_{\text{inj}}} \quad (14)$$

Next, to ensure that the injected oil was mixed at the impeller without overshooting, the fluid velocity at the impeller must be higher or equal to the feed velocity, as shown in Equation 15.

$$\frac{Q_{\text{imp}}}{A_{\text{imp}}} \geq \frac{Q_{\text{feed}}}{A_{\text{pipe}}} \quad (15)$$

where:  $Q_{\text{imp}} = N_Q N_{jd} D^3$  and  $A_{\text{imp}} = \pi \frac{D^2}{4}$

The oil was added using a ISMATEC, MCP-Z standard gear pump with mounted suction shoe pump head. A metal feed pipe was used to ensure that the injection point was stationary.

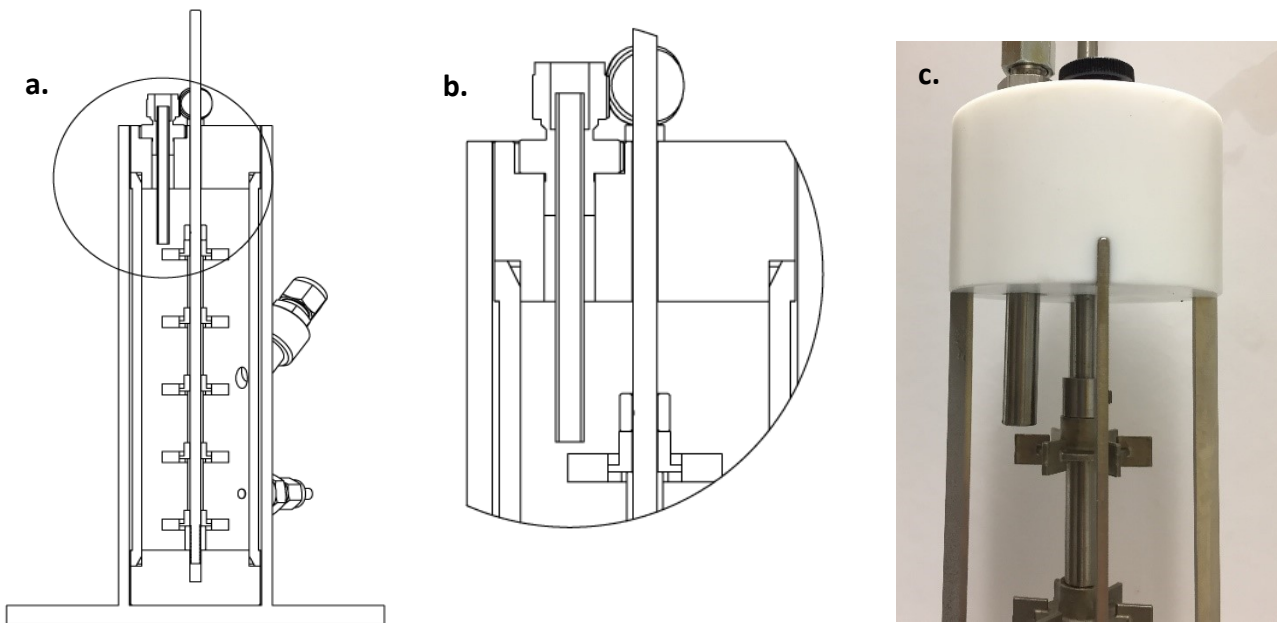


**Figure 6- Feed pipe experimental setup. (a) Schematic drawing of CIST with FBRM port and feed pipe. (b) Close up of the feed pipe at the first impeller. (c) Image of feed pipe and the top impeller. The center of the pipe was at  $r/R=0.85$  and the length of the feed pipe was 3.5 cm.**

Impeller feed experiments were only performed in the CIST at 10% holdup. At 30% holdup in the CIST, the top impeller was suspended in the air for part of the injection process. For the ST, the required rate of oil injection to meet the  $t_{cd}$  specification was faster than the capacity of available pumps.

For each geometry, the pump and FBRM software were started simultaneously to record the transient chord length while the feed was injected. The chord length measurement was continued long enough after the feed was completely added to ensure that equilibrium was reached.

### 3 Results and Discussion

The results obtained from this study are presented in five sections. First, the effect of impeller type, dispersed phase holdup and the tank geometry on the points of initial and complete drawdown are summarized and the scaling of  $N_{cd}$  with power and energy is investigated. Next, the equilibrium time is defined using the transient chord length distribution and the mean chord length. Third, the transient Sauter mean chord length is calculated using the measured CLD data for all geometries (SL-ST, SL-CIST and IF-CIST) at both 10% and 30% holdups. Results obtained from surface layer experiments are compared with impeller feed experiments to understand the effect of feeding method on the chord length distribution. Finally, the effect of operating parameters on the Sauter mean chord length at the complete drawdown and equilibrium conditions is investigated to determine the accuracy of scaling the equilibrium chord length with power per mass (W/kg) vs. scaling the transient chord length with energy per mass (J/kg) across several geometries.

#### 3.1 $N_{id}$ , $N_{cd}$ and $t_{cd}$ Results

The first part of the study is focussed on the rotational speed needed to just-drawdown the liquid. While most previous studies report the point at which all of the fluid is completely drawn-down ( $N_{cd}$ ), the point of initial dispersion ( $N_{id}$ ) is also reported here. Given  $N_{cd}$ , the time required to reach complete drawdown at  $N_{cd}$  ( $t_{cd}$ ) was measured for a number of different geometries.

The experimental results for  $N_{id}$ ,  $N_{cd}$ , and  $t_{cd}$  are summarized in Table 3.

**Table 3- Initial drawdown speed ( $N_{id}$ ), complete drawdown speed ( $N_{cd}$ ) and drawdown time ( $t_{cd}$ ) for CIST and ST**

Impeller/Holdup	CIST				ST			
	$N_{id}$	$N_{cd}$	$N_{cd} - N_{id}$	$t_{cd}$	$N_{id}$	$N_{cd}$	$N_{cd} - N_{id}$	$t_{cd}$
	(rpm)	(rpm)	(rpm)	(s)	(rpm)	(rpm)	(rpm)	(s)
<b>RT-10</b>	250	650	400	86	50	115	65	180
<b>RT-30</b>	120	325	205	76	30	140	110	150
<b>PBT-DU-10</b>	275	700	425	270	-	-	-	-
<b>PBT-DU-30</b>	170	925	755	45				
<b>PBT-UD-10</b>	235	875	640	90				
<b>PBT-UD-30</b>	140	410	270	270				
<b>PBT-DD-10</b>	275	800	525	120	45	190	100	150
<b>PBT-DD-30</b>	170	410	240	266	53	240	187	420
<b>A310-10</b>	375	N.A.	1725	N.A.	110	280	170	420
<b>A310-30</b>	335	N.A.	1765	N.A.	60	300	240	510

*The point of initial drawdown ( $N_{id}$ ) and complete drawdown ( $N_{cd}$ )*

The point of initial disruption occurs at a much lower  $N$  in the ST than the CIST, with the interface disrupted at  $N$  which is 4-5 times smaller in the ST. Converting  $N$  to tip speed highlights the complexity of the flow field: the tip speed of the impeller does not scale the point of initial dispersion. In the CIST  $N_{id}$  is always smaller for the 30% hold-up cases (the top impeller is

submerged at 30% hold-up), while in the ST this is true for all but the PBTD (the interface is closer to the impeller). The difference between  $N_{cd}$  and  $N_{id}$  ( $N_{cd}-N_{id}$ ) is significantly larger for the CIST than the ST, ranging from 205 to 755 rpm for the CIST and ranging from 65 to 187 rpm for the ST. This is somewhat surprising, since the flow and turbulence are more uniform in the CIST. The completely drawdown rotational speed ( $N_{cd}$ ) was very different across the geometries tested, ranging from 115 rpm to 925 rpm with one case where complete drawdown could not be achieved (A310 in CIST). This wide range of  $N_{cd}$  indicates that the rotational speed alone is not sufficient to characterize the drawdown.

Comparing the effect of holdup on  $N_{cd}$  in the CIST and the ST shows that increasing the holdup from 10% to 30% increases  $N_{cd}$  in the ST, as more energy is required to drawdown the dispersed phase. However, when the holdup is increased in the CIST,  $N_{cd}$  drops. The difference observed between the ST and CIST at 30% holdup can be explained by considering the level of the liquid layer, as shown in Figure 3. In the CIST at 30% holdup the top impeller is submerged into the oil phase and as a result, dispersion of the interface occurs at a much lower rotational speed and enhances the drawdown of the oil. This result suggests that the liquid level relative to the impeller location is an essential consideration in the mixing system design.

#### *Effect of holdup and geometry on $t_{cd}$*

The final column of data in 3 for each vessel geometry is the time needed to achieve complete drawdown,  $t_{cd}$ . The largest change in  $t_{cd}$  with a change in geometry at a single holdup (86 s to 420s) is larger than the largest change in  $t_{cd}$  with a change in holdup in a single geometry (45 s to 270s). Within a single geometry, changing the holdup did not have a consistent effect on  $t_{cd}$ . Considering the position of the impeller relative to the liquid interface also does not provide any satisfying explanation for the variation in  $t_{cd}$  data.

When the A310 impeller was used in the CIST at either 10% or 30% holdup, complete drawdown could not be achieved even at the maximum possible rotational speed ( $N=2100$  rpm). After 30 min of mixing, large drops of unmixed oil were still visible at the top of the vessel close to the baffle. Thus,  $t_{cd}$  is not reported for these cases.

*Correlation of  $N_{cd}$  with power and energy*

The correlation of point of complete drawdown ( $N_{cd}$ ) with the *measured* power per mass is presented in Figure 7.

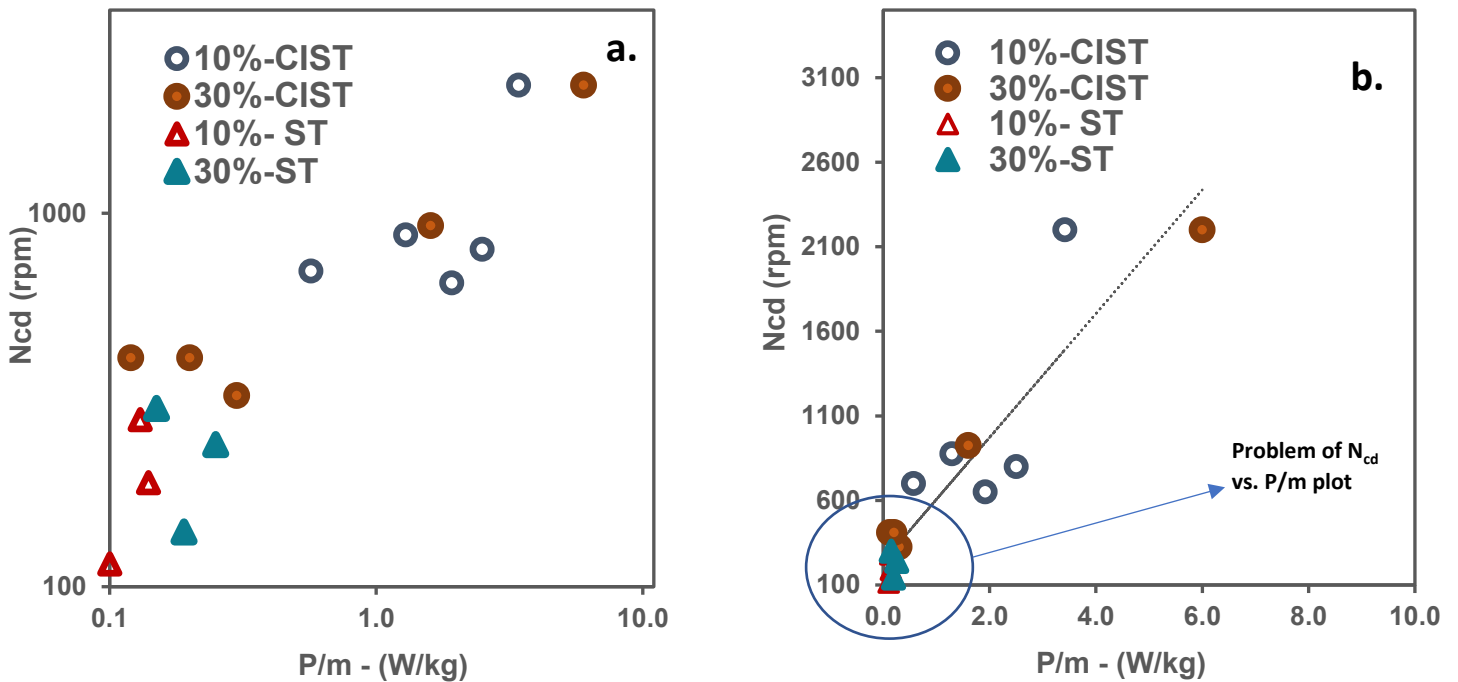


**Figure 7-  $N_{cd}$  vs. measured power per mass ( $P/m$ ), (a) log-log plot (b) normal plot**

The power was calculated from torque measurements (using the method reported by (Chapple et al. 2002)) and  $N_{cd}$ , and normalized with the total mass of the liquid in each vessel.

$$\frac{P}{m} = \frac{2\pi N_{cd} T_q}{m} \quad (16)$$

The results are given in Table 3 and show that the power consumption at the point of complete drawdown depends on the tank geometry, (CIST, ST), impeller type (RT, A310, PBT) and holdup covering a range from 0.1 to 3.4 W/kg. This is in agreement with work by (Ghotli et al. 2013) who reported that the power consumed depends on the tank geometry and impeller type. In this table, the arrow points toward the larger number of the 10%/30% hold-up pair. We note that for the ST, the P/m always increases with hold-up, while in the CIST, it may either increase or decrease with increasing hold-up.

$N_{cd}$  is plotted vs power per mass (P/m) in Figure 7. In the linear plot (a), the data is scattered and in the log-log plot (b), the data is clustered at the origin. We conclude that  $N_{cd}$  does not scale with the power per mass (P/m).

**Table 4- Energy consumed for the complete drawdown normalized to the ST-RT-10**

Impeller/Holdup	Normalized P/m		Normalized $J_{cd}/m$	
	10%	30%	10%	30%
Rushton – ST	1 →	1.9	1 →	1.5
Rushton – CIST	19.2 ←	3	9.4 ←	1.2
PBT – ST	1.4 →	2.5	1.2 →	5.8
PBT – CIST - UD	12.9 ←	1.2	6.7 ←	1.9
PBT – CIST - DU	5.7 ←	16	8.8 ←	4.3
PBT – CIST - DD	25 ←	2	17 ←	2.8
A310 – ST	1.3 →	1.5	2.9 →	4.2
A310 – CIST	34.2	60	-	-

As the power per mass does not capture a consistent scaling for this system, the energy per mass ( $J_{cd}/m$ ) which is the product of power and drawdown time (Equation 17), was considered. The power per mass  $P/m$  is the point wise energy needed to completely drawdown the dispersed phase, while  $J/m$  is the cumulative energy added to the system. Because the cumulative energy is time dependent, it is more likely to characterize the system dynamics.

$$\frac{J_{cd}}{m} = \frac{P * t_{cd}}{m} \quad (17)$$

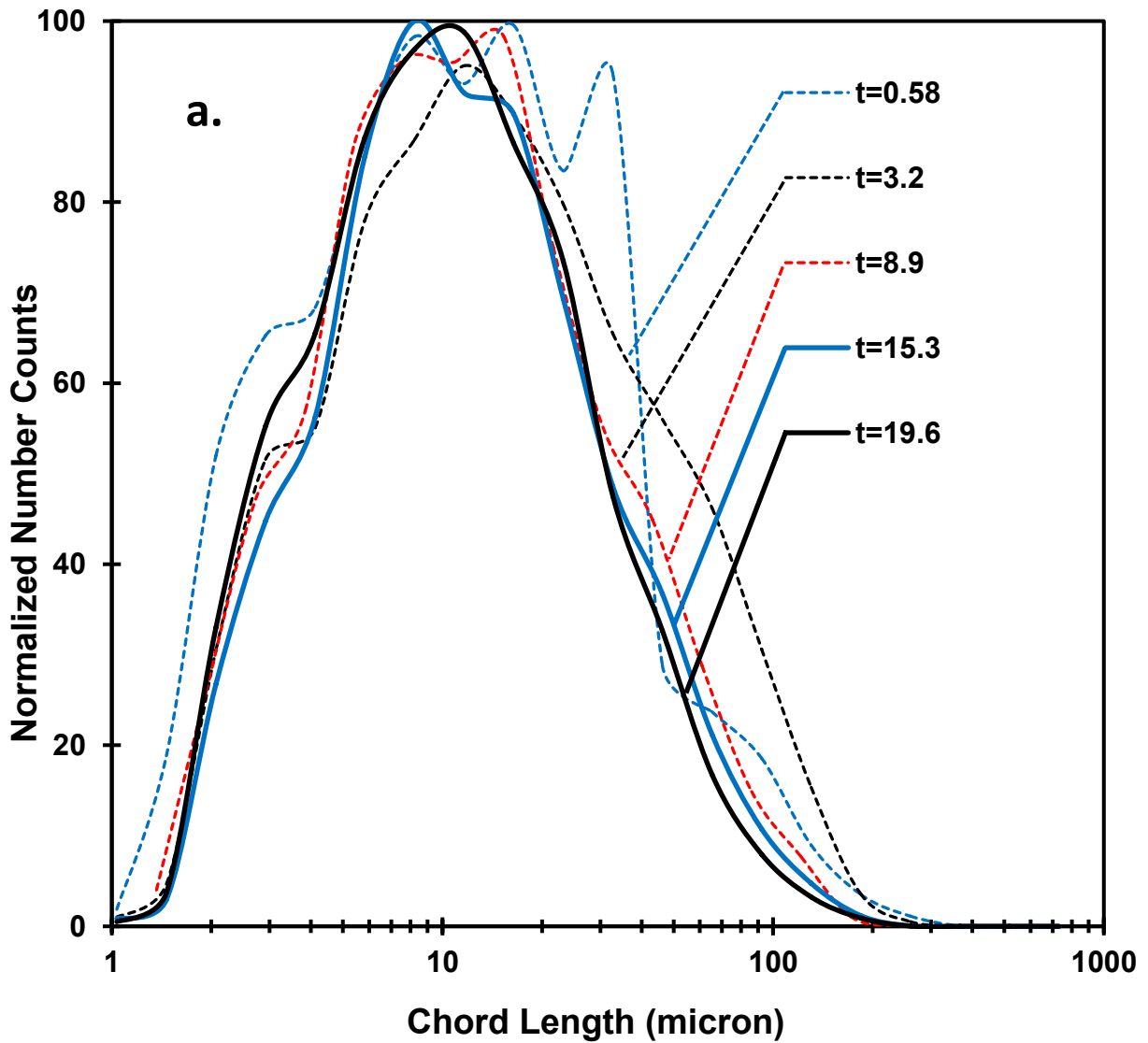
$J_{cd}/m$  was normalized to the base case of a Rushton impeller in the ST at 10% holdup. When holdup is increased, the ST consumes more energy as expected, but the CIST consumes less energy. This result was initially puzzling until the position of the interface relative to the top impeller is compared in Figure 3. At 30% holdup, the top impeller is submerged in the second phase in the CIST, but not in the ST. This accelerates the drawdown of oil and results in lower energy consumption.

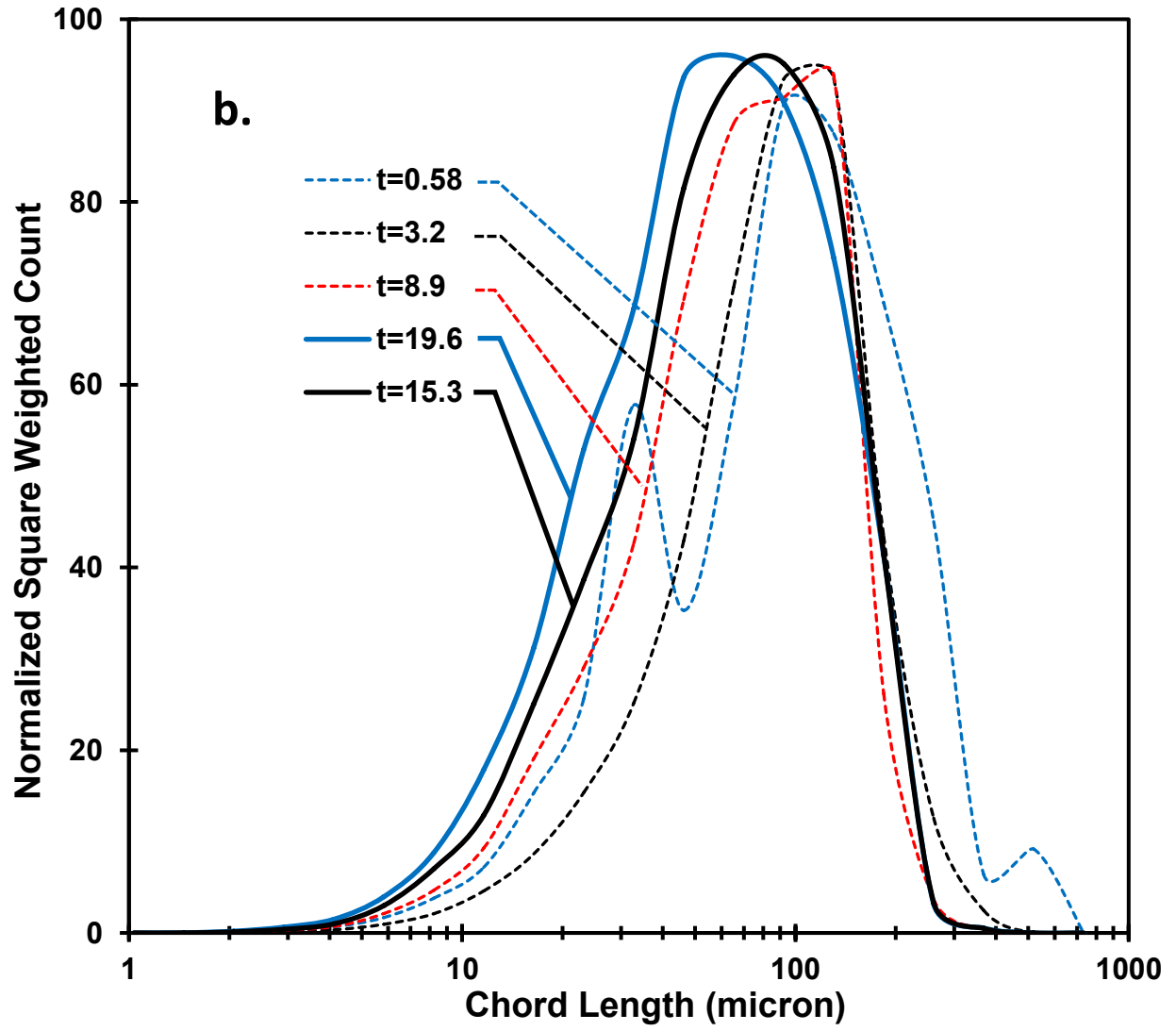
Based on the ranges and trends in  $N_{id}$ ,  $N_{cd}$  and  $t_{cd}$ , and the lack of clear correlations in the data for both  $P/m$  and  $J/m$ , a new hypothesis is proposed: the wide range of energy consumed at the complete drawdown time ( $t_{cd}$ ) may result in differences in the chord length (or drop size distribution). Geometries with higher  $J_{cd}$  were predicted to result in smaller chord length. To test this hypothesis, the transient chord length distribution was measured, the Sauter mean chord length ( $cl_{32}$ ) was calculated and the correlation of  $cl_{32}$  with power and energy was examined.

### 3.2 Chord Length Distribution and $teq$

To investigate the evolution of the chord length distribution over the time, the transient chord length distribution was measured at  $N_{cd}$  using the FBRM. Figure 8 presents the number, square

weighted and cumulative distributions for the surface layer experiment with PBT- DU impellers at 30% holdup in the CIST (SL-CIST- DU-30) at the beginning of the mixing process (from  $t=0$  to  $t=19.6$  s). As the total number of counts was not the same in the different geometries, all distributions were normalized to the total count. Each color represents a single point in time. As expected, the distributions were broad and scattered and the square weighted distribution was shifted towards the bigger drops.





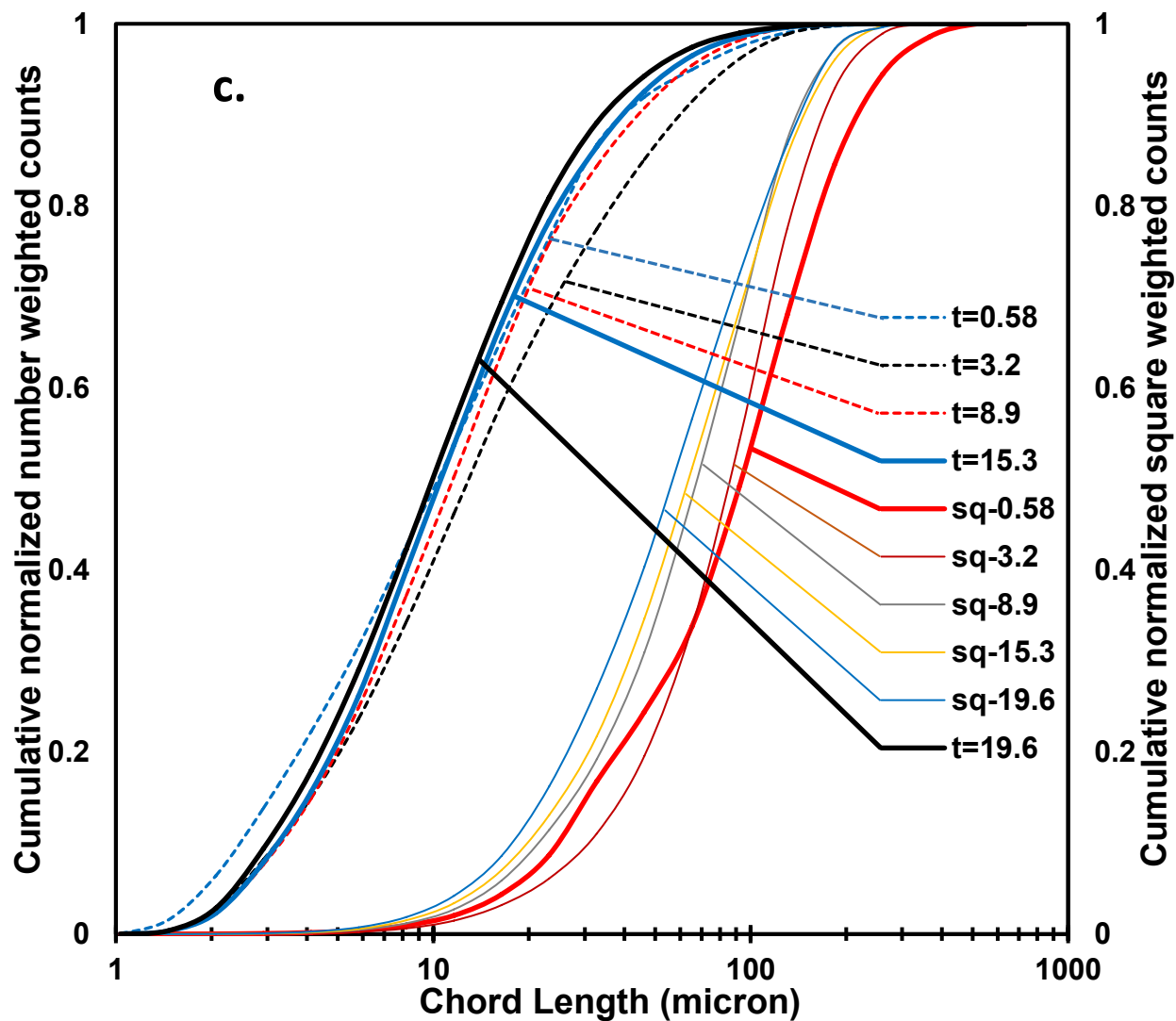
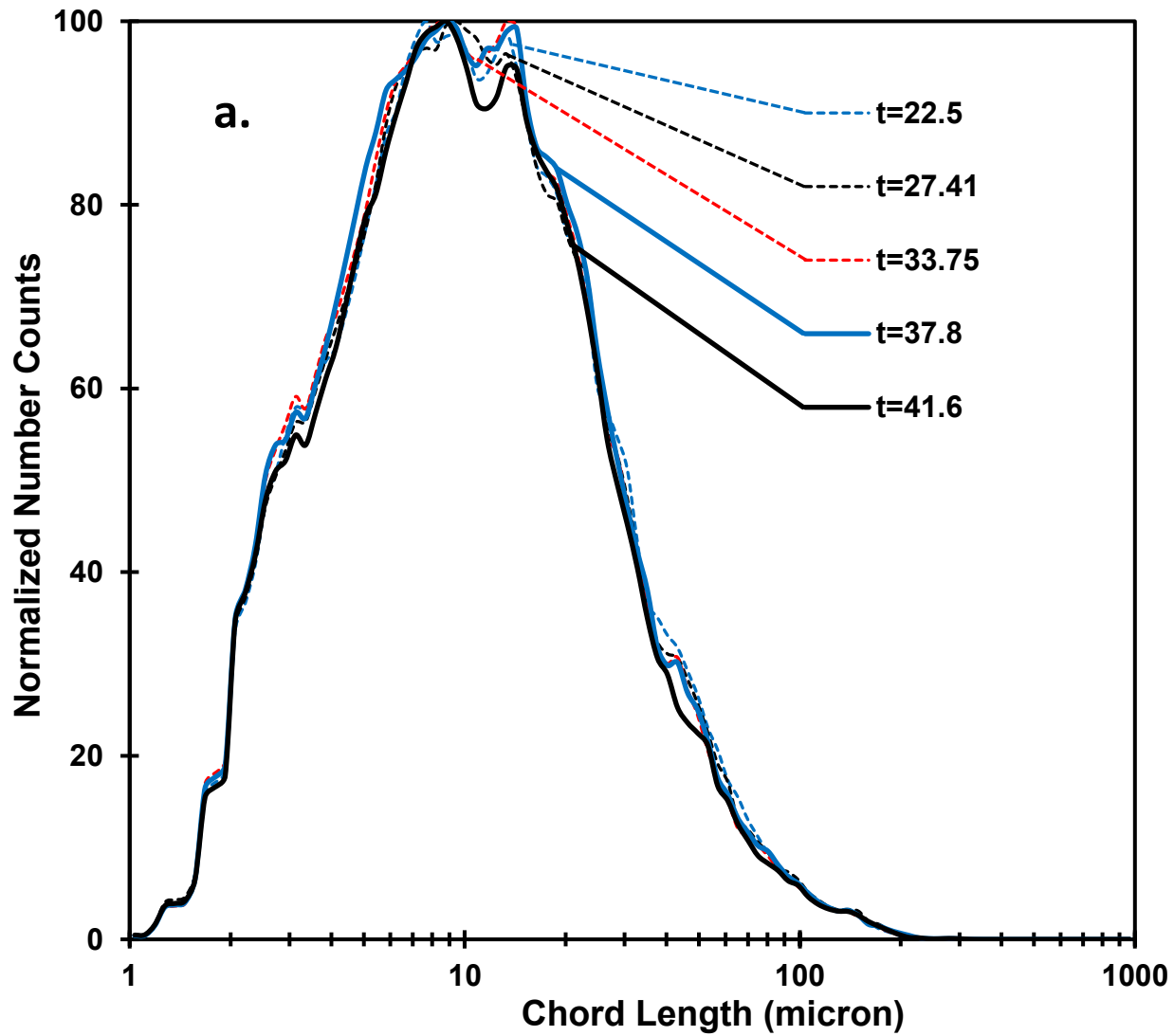


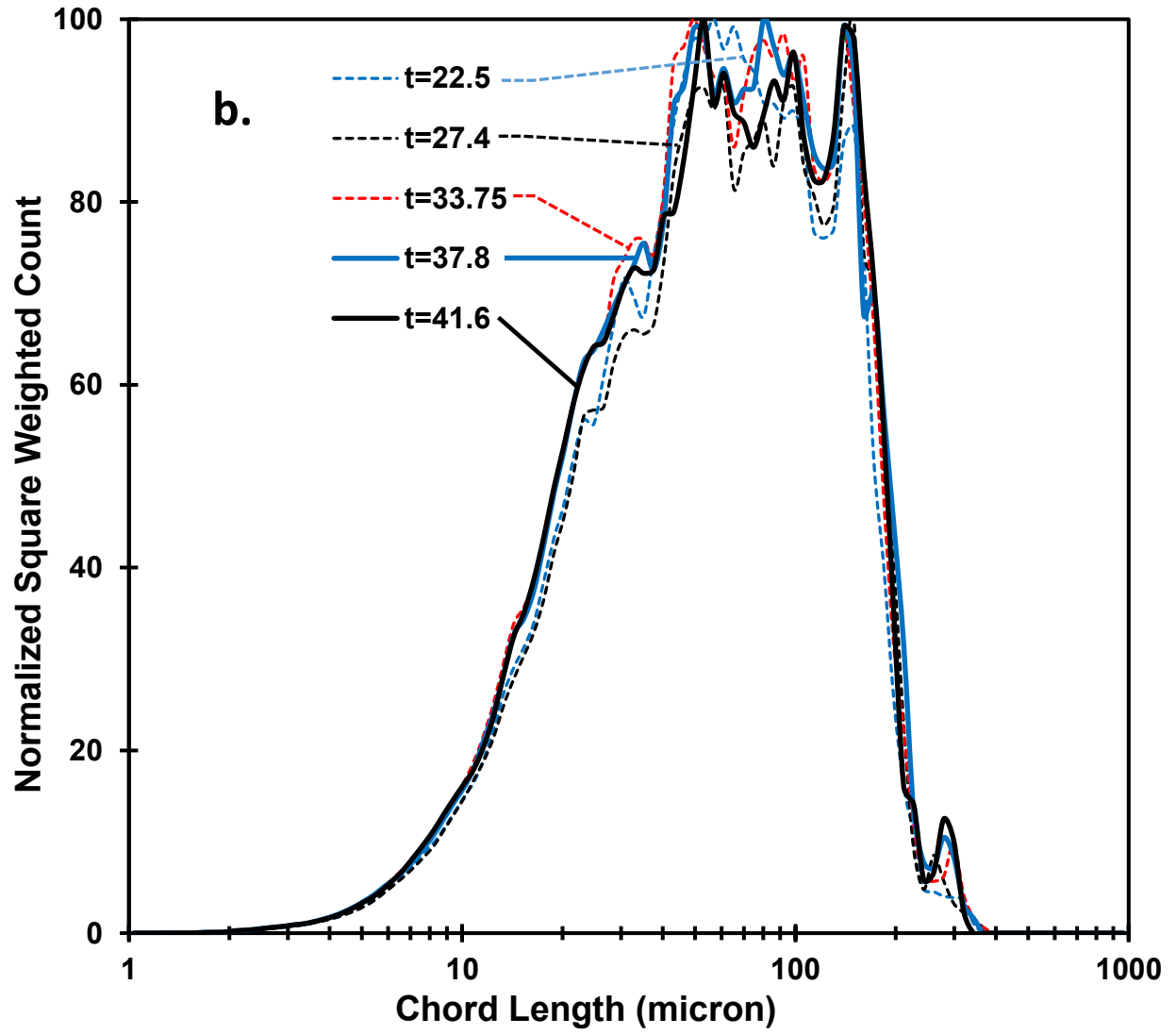
**Figure 8- (a) Number (b) Square weighted and (c) Cumulative chord length distribution (number weighted on left vertical axis and square weighted on right) for CIST-PBT DU-30 at the beginning of mixing process (from  $t=0$ )**

The equilibrium time ( $t_{eq}$ ) is the time after which the chord length distribution and the mean drop size remain unchanged. Other authors have shown that the equilibrium time depends on the mixing conditions and the physical properties of both liquids (Hong & Lee 1983a; Ceylan et al. 2003; Poblete et al. 2016). Figure 9 presents the number weighted, square weighted and cumulative CLD

distributions for the CIST-DU-30 in the surface layer experiment. After the equilibrium time, all distributions are stable for the rest of the experiment. Comparing the distributions before and after equilibrium (

Figure 8 and Figure 9) shows that the chord length distribution is broad at the beginning and gradually narrows down as dynamic steady state is approached. The same behaviour was observed for the other test configurations (16 surface layer and 5 impeller feed). This result is in agreement with previously reported data on the DSD (Hong & Lee 1983a). They also observed that the DSD was broad at the beginning and narrowed down as the equilibrium DSD approached.





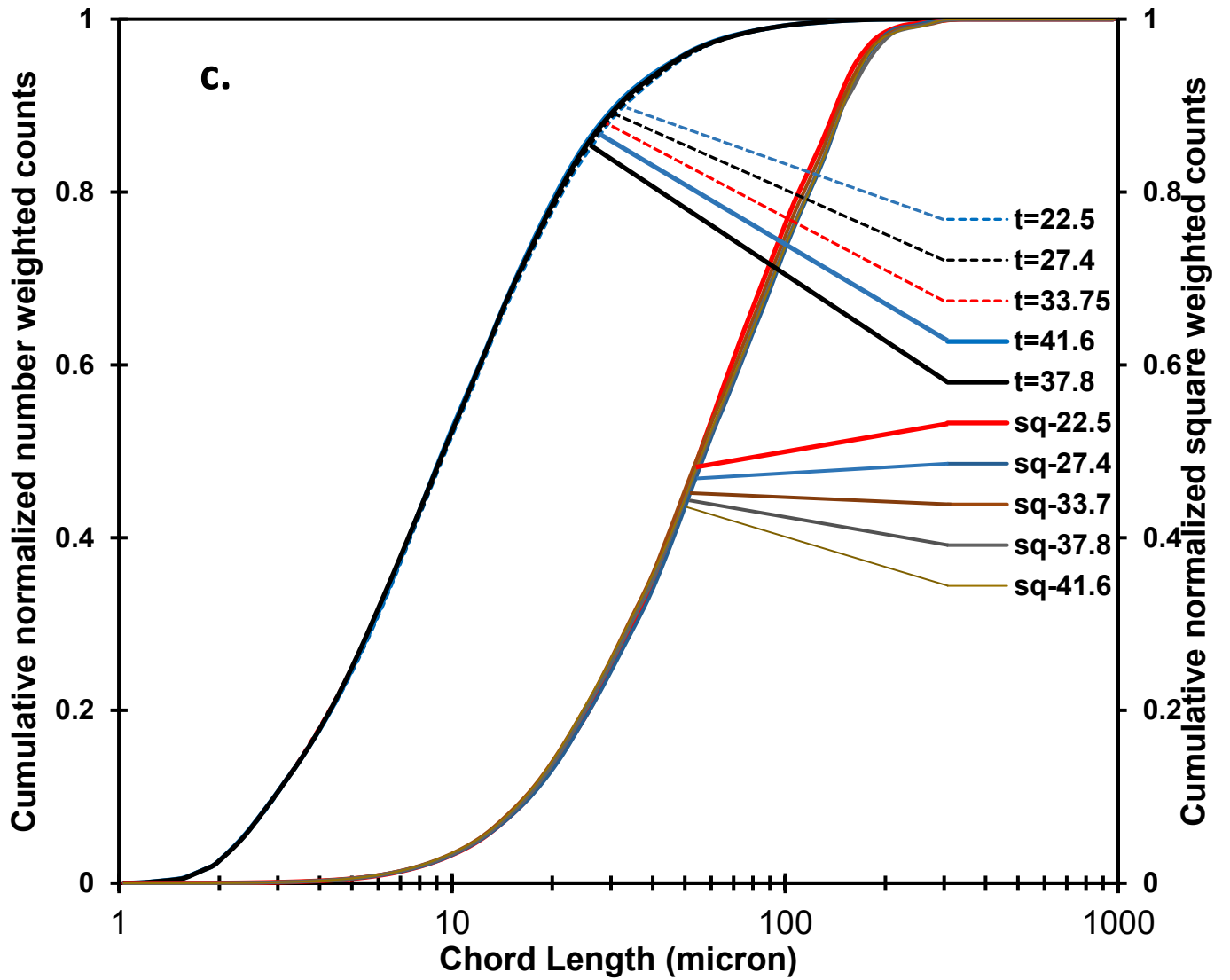


**Figure 9- (a) Number (b) Square weighted and (c) Cumulative chord length distribution for CIST-PBT DU-30 after equilibrium**

Two definitions of  $t_{eq}$  are reported in the literature (Chatzi, Costas J Boutris, et al. 1991; Hong & Lee 1983b). In the first method, the transient drop size distribution is observed and the equilibrium time is visually defined as the time after which there are no significant changes in the transient DSD. In the second method, the equilibrium time is defined based on the transient Sauter mean

drop size ( $d_{32}$ ). The time after which the fluctuation of  $d_{32}$  was less than the desired value (e.g. 5%) was defined as the equilibrium time. The Sauter mean drop size,  $d_{32}$ , is the ratio of the third to second moments of DSD.

$$d_{32} = \frac{\sum_{i=1}^{i=k} n_i d_i^3}{\sum_{i=1}^{i=k} n_i d_i^2} \quad (18)$$

In this study, both methods were used. First, the number weighted, square weighted and cumulative CLD distributions were plotted. The time after which all the distributions remained unchanged was defined as  $t_{eq1}$ . Next, the transient Sauter mean chord length ( $cl_{32}$ ) was plotted (Figure 10, Figure 11, Figure 12, Figure 14) and the time after which the fluctuations of the transient  $cl_{32}$  were minimal, and was considered as the  $t_{eq2}$ . For each geometry, the larger of  $t_{eq1}$  or  $t_{eq2}$  was defined as the equilibrium time. The difference between  $t_{eq1}$  and  $t_{eq2}$  ranged from 0 to 45%. Table 5 presents the equilibrium time for the CIST and the ST in both surface layer and impeller feed experiments.

**Table 5- Equilibrium time (max of  $t_{eq-1}$  and  $t_{eq-2}$ ) for surface layer and impeller feed experiments**

Impeller/Holdup	Surface Layer (SL)		Impeller Feed (IF)
	CIST	ST	CIST
	$t_{eq}$ (s)	$t_{eq}$ (s)	$t_{eq}$ (s)
<b>RT-10</b>	1560	2160	1740
<b>RT-30</b>	2220	1680	-
<b>PBT-DU-10</b>	1980	2100	1020
<b>PBT-UD-10</b>	1860		1680
<b>PBT-DD-10</b>	2400		1800
<b>PBT-DU-30</b>	1560	1680	-
<b>PBT-UD-30</b>	2160		-
<b>PBT-DD-30</b>	2340		-
<b>A310-10</b>	1440	2100	1080
<b>A310-30</b>	1500	1800	-

For the Rushton impeller with 10% holdup (CIST and ST, surface layer and impeller feed experiments), the chord length continuously decreased even after 1hr of mixing. The same result was observed for the CIST-PBT-DU-10. In these cases, the equilibrium time was defined from 3 distribution graphs, although the breakup remained the dominant process.

In some geometries, bi-modal and tri-modal CLDs were observed (e.g. SL-CIST-RT-10) as previously reported by Chatzi et al. (1991), who observed a bimodal DSD for styrene in water drawdown when impeller was used at 300 rpm, which was higher than the  $N_{cd}$  for their system.

They commented that the multi-modal (or polydisperse) distributions indicate that more than one breakup/coalescence mechanism controls the drop size.

### **3.3 Transient Sauter Mean Chord Length ( $cl_{32}$ ) Analysis**

The transient Sauter mean chord length was calculated for all experiments. In these figures, the filled and empty circles on the graph indicate  $t_{cd}$  and  $t_{eq}$  respectively. Transient  $cl_{32}$  data was analyzed from the beginning of the mixing to the point of complete drawdown ( $0 < t < t_{cd}$ ) and from the point of complete drawdown until the equilibrium was reached ( $t_{cd} < t < t_{eq}$ ). It is clear that  $t_{eq}$  is much longer than  $t_{cd}$ . The effects of geometry (ST vs CIST), holdup (10% vs 30%), and feeding method (surface drawdown vs impeller feed) on the transient  $cl_{32}$  are evaluated in the following sections.

#### **3.1.1 Transient $cl_{32}$ for ST**

The calculated  $cl_{32}$  for both 10% and 30% holdup in the ST is presented in Figure 10. Most of the changes in the mean chord length occur during the initial drawdown ( $t < t_c$ ) when  $cl_{32}$  exponentially decreases to reach a near equilibrium length at  $t_{cd}$ . The change in  $cl_{32}$  from  $t_{dc}$  to  $t_{eq}$  was less than 10% for most of the stirred tank cases. Equilibrium was reached after approximately 1800 s for all cases and after reaching equilibrium, noticeable fluctuations around the mean were frequently observed, indicating a dynamic equilibrium rather than a fixed distribution.

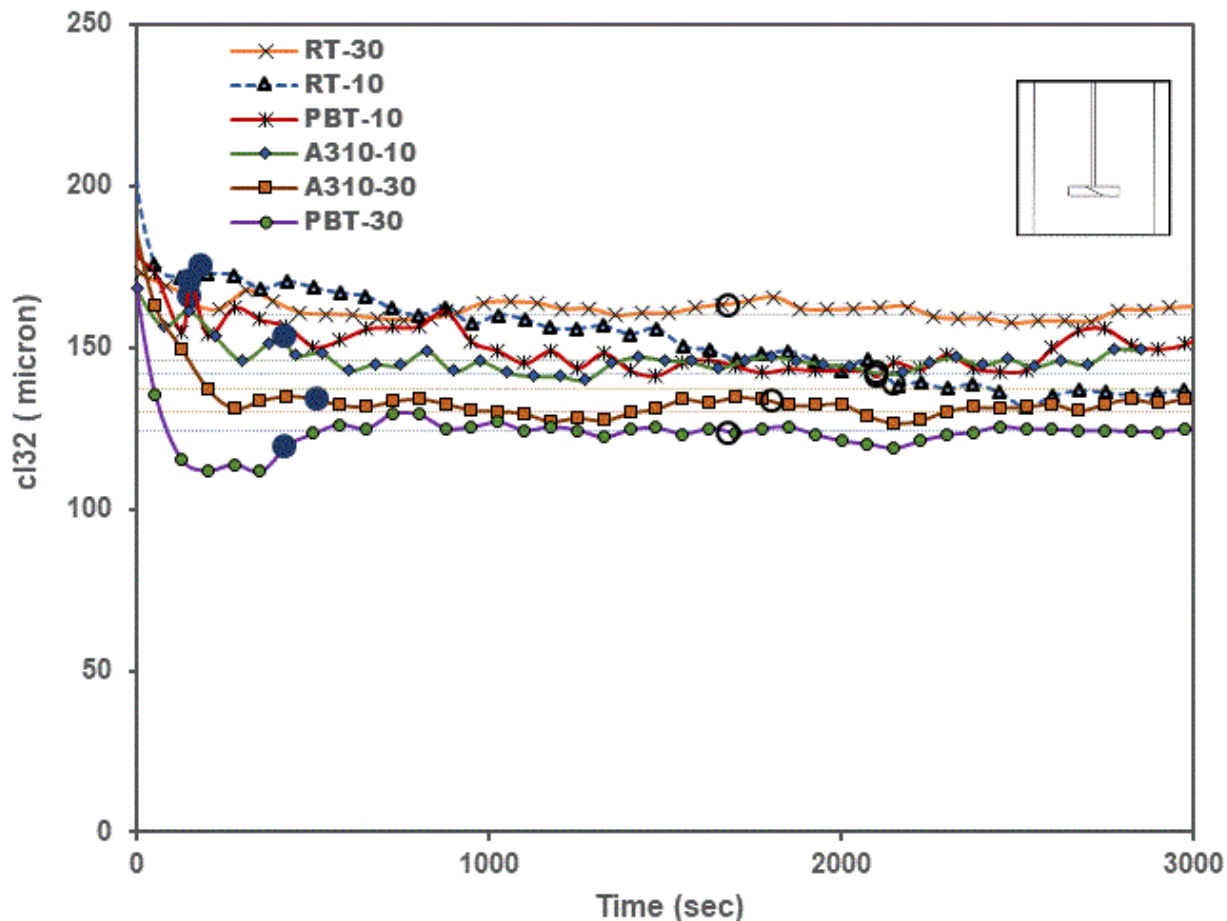


**Figure 10- Transient Sauter mean ( $cl_{32}$ ) for surface layer at  $\phi=10\%$  and  $30\%$  in ST. Dotted lines are equal to the equilibrium  $cl_{32}$ . The filled and empty circles are  $t_{cd}$  and  $t_{eq}$  respectively**

The effect of holdup on the Sauter mean chord length in the ST did not show a clear trend. When a Rushton impeller was used,  $cl_{32}$  increased by increasing the holdup while for PBT and A310,  $cl_{32}$  decreased by increasing the hold up. The maximum  $cl_{32}$  was  $160 \mu\text{m}$ , observed for the RT-30 and the minimum  $cl_{32}$  was  $120 \mu\text{m}$ , observed for the PBT-30.

To further investigate the effect of vessel geometry and feed conditions, the transient Sauter mean chord length was also calculated for the CIST for both surface layer and impeller feed.

### 3.1.2 Comparison of Surface Drawdown and Impeller Feed

Figure 11 and Figure 12 show the  $cl_{32}$ -time plot for the CIST at 10% holdup with surface layer and impeller feed respectively. The RT with impeller feed (Figure 12) shows a significantly different trend than the other curves, so this run was repeated. The results were consistent.

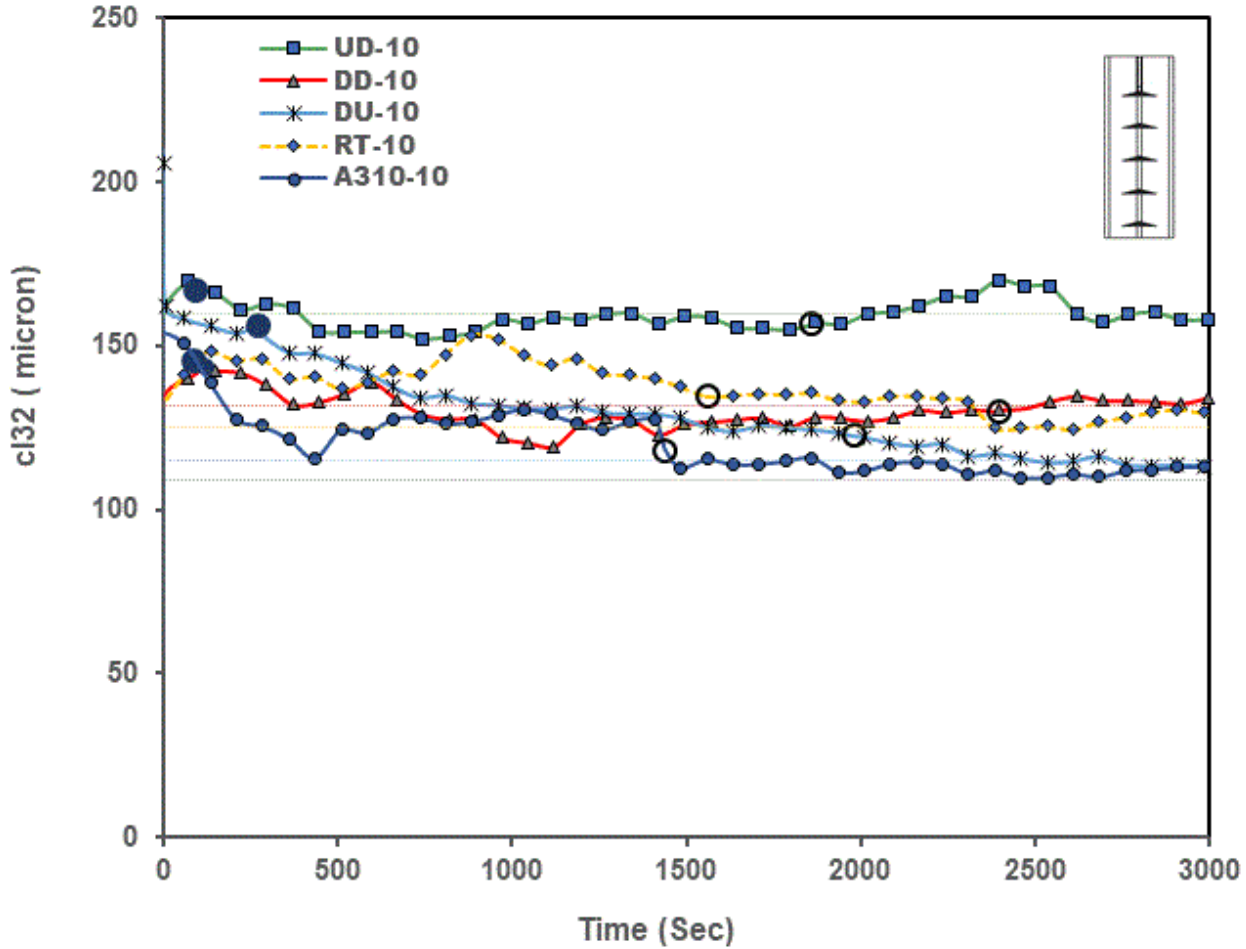
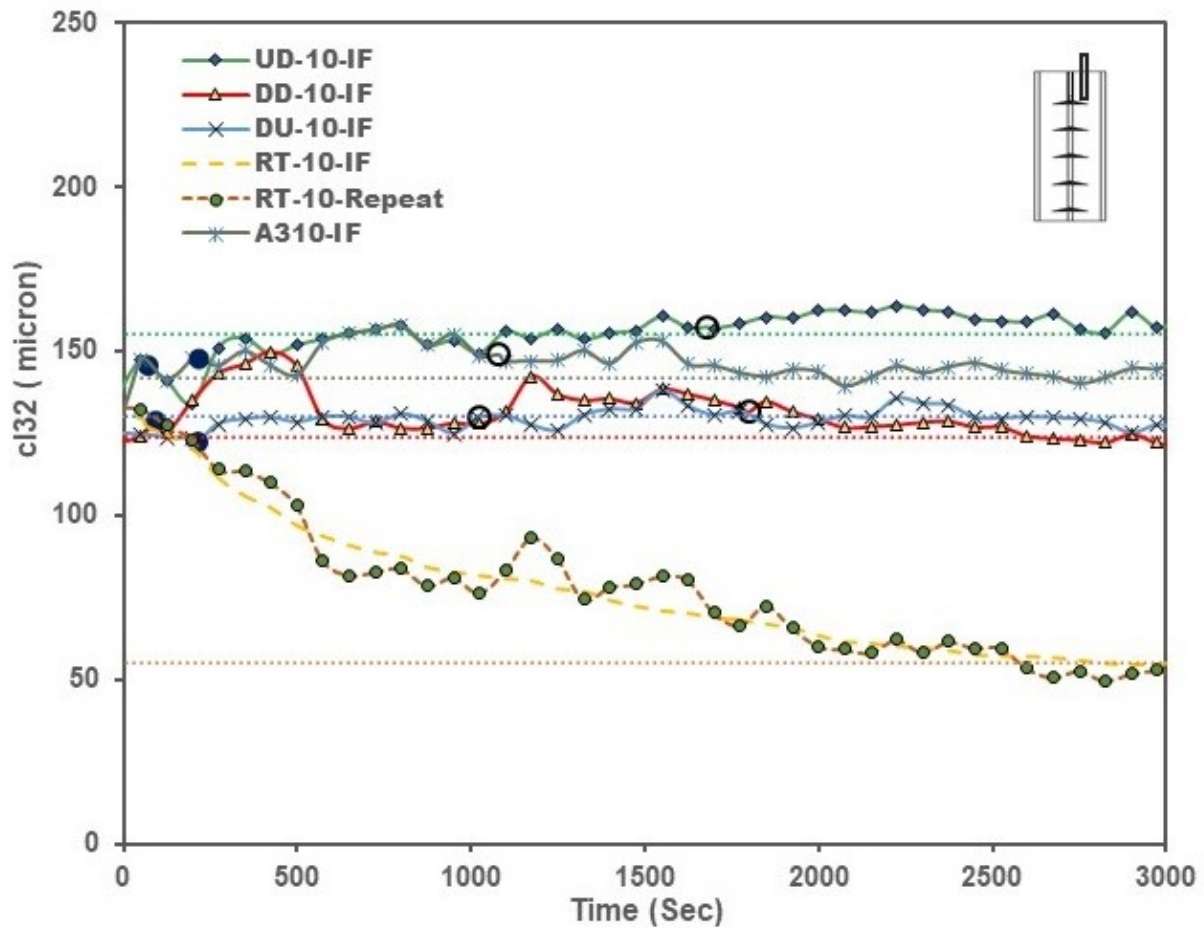


Figure 11- Transient Sauter mean ( $cl_{32}$ ) for surface layer at  $\phi=10\%$  in CIST. The first and second dots are  $t_{cd}$  and  $t_{eq}$



**Figure 12- Transient Sauter mean ( $cl_{32}$ ) for impeller feed at  $\phi=10\%$  in CIST. The filled and open dots are  $t_{feed}$  and  $t_{eq}$ .**

### 3.1.3 Comparison of Equilibrium Time

Comparison showed that in the surface layer experiments, equilibrium happened after 25 min, while in the impeller feed,  $t_{eq}$  happened after 17 min. Impeller feed reached equilibrium faster as the initial time required for the drawdown of the oil into the water was reduced by injecting the oil into the water phase.

In the both surface layer and impeller feed, after  $t_{eq}$ , the oscillation of  $cl_{32}$  was observable, indicating that equilibrium was dynamic. However, these fluctuations were more significant for the surface layer, and much more stable for the impeller feed. The fluctuations around the equilibrium drop size were also larger in the ST than in the CIST. The equilibrium drop size is most stable in the CIST with feed at the impeller. Note that impeller feed in the ST was not possible in this study.

### **3.1.4 Effect of Impeller Geometry and Feed on the CLD**

To compare the effect of impeller geometry on the transient mean chord length and the equilibrium chord length distribution, two representative geometries are compared in Figure 13. The PBT-UD gives a similar equilibrium Sauter mean chord length ( $cl_{32-eq}$ ) for the impeller feed and surface layer, which is true for all three configurations of UD, DD and DU. When the RT is used, the impeller feed generates a smaller  $cl_{32}$  and smaller  $cl_{32-eq}$  (132  $\mu\text{m}$  for the surface layer vs 60  $\mu\text{m}$  for the impeller feed) while this trend is reversed for the A310, where the surface layer generates smaller drops.

The notable difference for the RT can be attributed to the highly localized energy dissipation at the impeller for the RT (Soos et al. 2013). When the oil is fed at the impeller, it is in direct contact with the high energy zone which results in rapid breakup and very small drops. For the surface layer, the dispersed phase does not always come to the intimate contact with the impeller. Thus, the  $cl_{32}$  for impeller feed is about 50% smaller than for the surface layer.

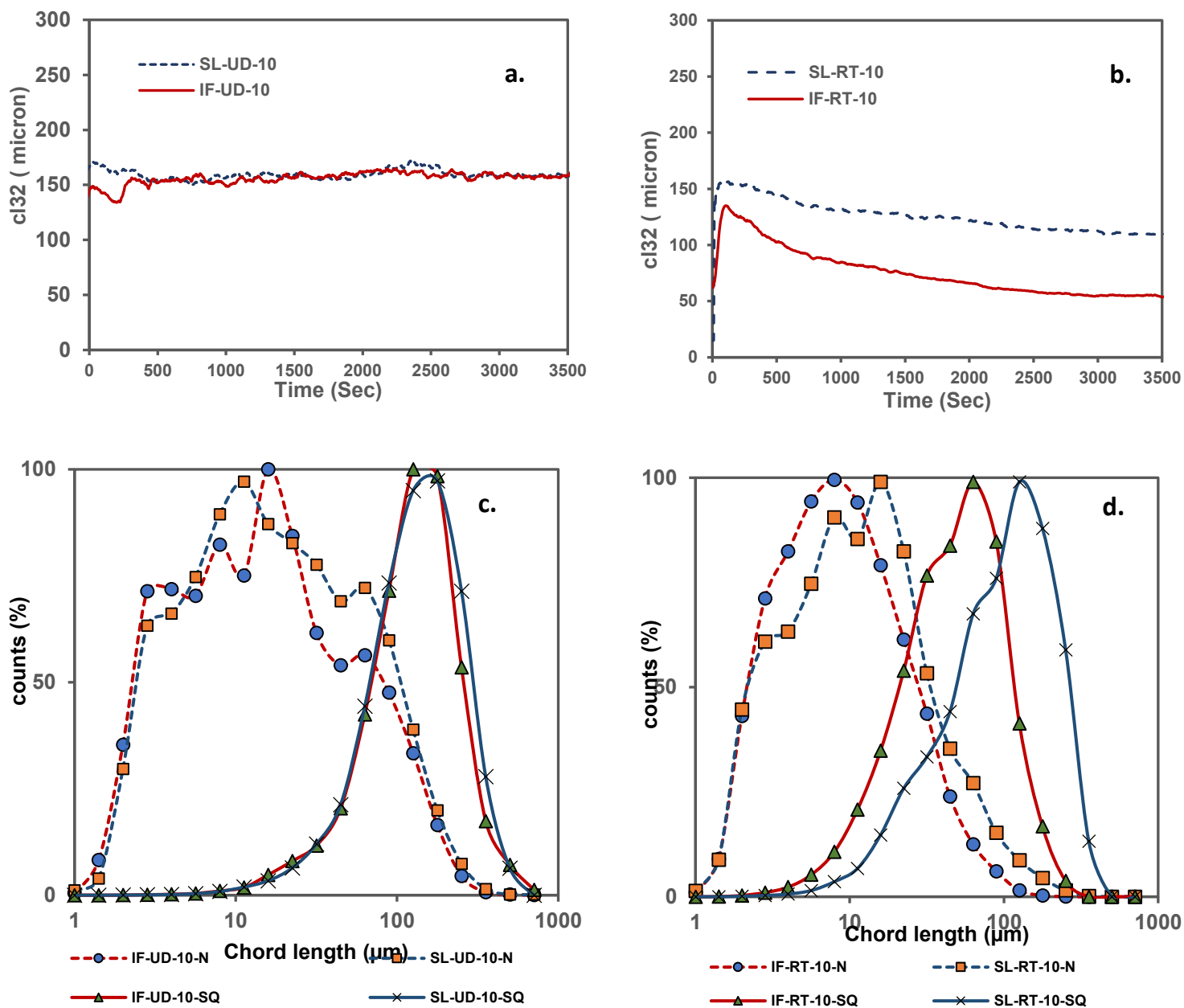


**Figure 13- Transient Sauter mean chord length ( $cl_{32}$ ) for impeller feed and surface layer in CIST (a) UD-10, (b) RT-10 and equilibrium chord length distribution of impeller feed and surface layer in CIST (c) UD-10, (d) RT-10**

### 3.1.5 Effect of Holdup on $cl_{32}$ in CIST

The transient Sauter mean chord length for 30% holdup in the CIST is given in Figure 14. Comparison of Figure 11 (10% holdup) and Figure 14 (30% holdup) shows that increasing the

holdup has a dramatic effect on the  $cl_{32}$ . For the CIST-10 and ST-10, the  $cl_{32,eq}$  covers a fairly narrow range, from 125-160  $\mu\text{m}$  while for the CIST-30,  $cl_{32,eq}$  ranges from 70-500  $\mu\text{m}$ . When the top impeller is submerged into the dispersed phase (Yeo et al. 2002) a local phase inversion may occur in which both water-in-oil drops and oil-in-water drops form. This additional dynamic of drawdown results in dramatic changes to the  $cl_{32}$  at equilibrium. The equilibrium time of 25 minutes is similar to that observed at 10% holdup.

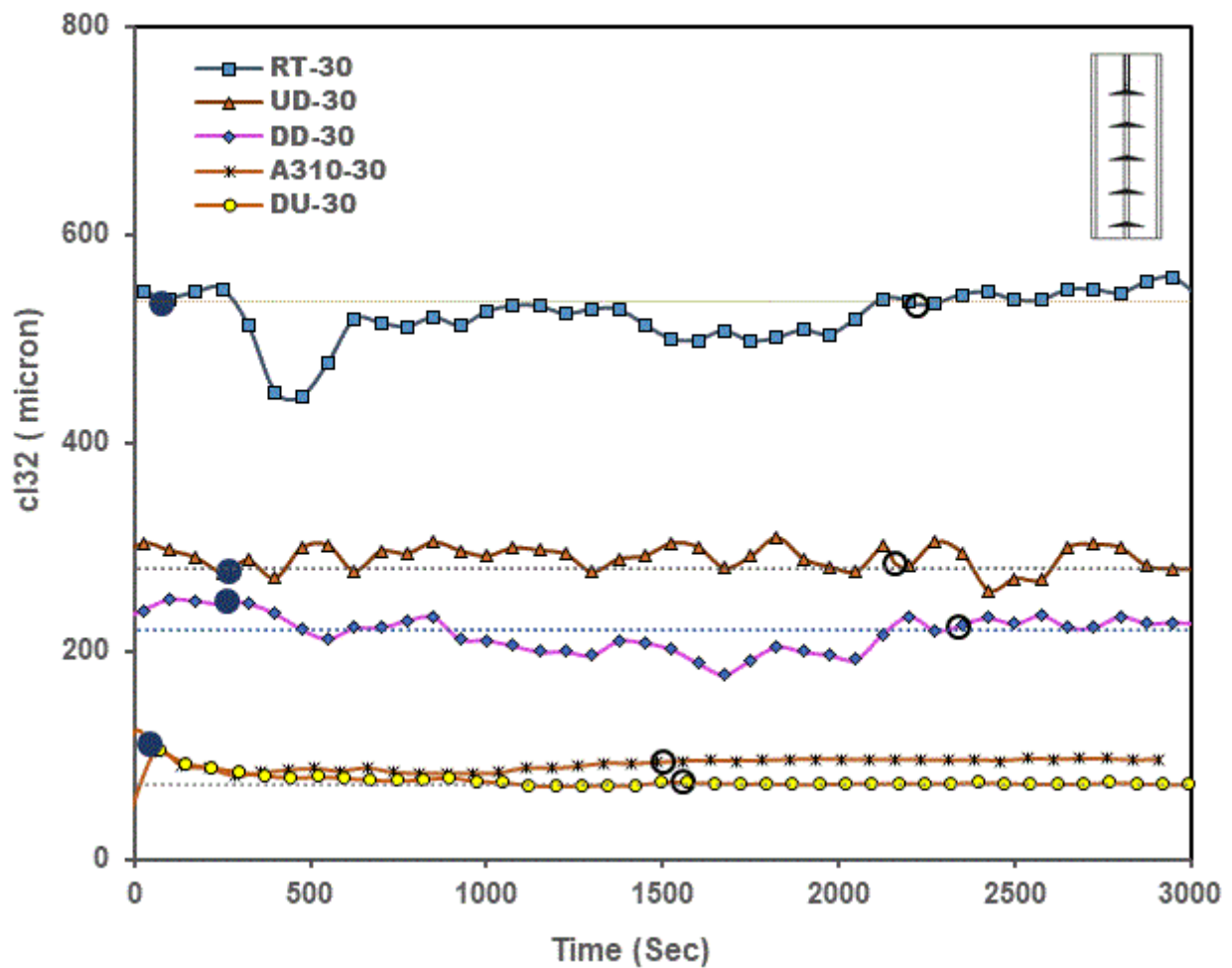


Figure 14- Transient Sauter mean ( $cl_{32}$ ) for surface layer at  $\phi=30\%$  in CIST. The first and second dots are  $t_{cd}$  and  $t_{eq}$

The key results from this section ( $cl_{32-cd}$  and  $cl_{32-eq}$ ) are summarized in Table 6. For the impeller feed experiments, the  $cl_{32-cd}$  is the  $cl$  at the end of the feed time. It is also generally accepted that increasing the impeller speed, decreases the drop size (Nishikawa et al., 1987, Kataoka et al., 1986, Poblete et al. 2016). Even this result appears restricted to cases where the geometry, feed location, and hold-up remain the same.

**Table 6- Equilibrium Sauter mean chord length ( $cl_{32-eq}$ ) and Sauter mean at the point of complete drawdown ( $cl_{32-cd}$ ) for Surface layer and at the end of feeding for Impeller feed experiments**

Impeller- Holdup	Surface Layer				Impeller Feed	
	CIST		ST		CIST	
	$cl_{32-cd}$ ( $\mu\text{m}$ )	$cl_{32-eq}$ ( $\mu\text{m}$ )	$cl_{32-cd}$ ( $\mu\text{m}$ )	$cl_{32-eq}$ ( $\mu\text{m}$ )	$cl_{32-cd}$ ( $\mu\text{m}$ )	$cl_{32-eq}$ ( $\mu\text{m}$ )
<b>RT-10</b>	146	132	172	140	136	60
<b>RT-30</b>	520	500	165	160	-	-
<b>PBT- DU-10</b>	151	135	166	150	130	132
<b>PBT- UD-10</b>	163	160			147	160
<b>PBT- DD-10</b>	140	130			138	125
<b>PBT- DU-30</b>	95	70	120	123	-	-
<b>PBT- UD-30</b>	300	300			-	-
<b>PBT- DD-30</b>	248	250			-	-
<b>A310-10</b>	-	125	150	146	147	145
<b>A310-30</b>	-	133	144	133	-	-

### 3.4 Comparison of the Mean Chord Length and Kolmogorov Length

Based on the Kolmogorov theory, the turbulent spectrum is divided into integral, inertial and viscous subrange. In the inertial subrange, inertial stress balances against the interfacial tension, while in the viscous subrange both inertial and viscous stresses play a role. Kolmogorov length scale ( $\eta$ ) defines the lower limit of the inertial subrange and is equal to  $(\frac{\nu^3}{\varepsilon})^{0.25}$ . In this equation,  $\varepsilon$  is the rate of energy dissipation and  $\nu$  is the kinematic viscosity of the continuous phase. The upper limit of the inertial subrange is defined by the integral scale,  $L$  which is in the order of  $D/10$  and  $D$  is the impeller diameter (Boxall et al. 2012). When the mean drop size is much larger than the Kolmogorov scale and much smaller than the integral scale ( $\eta < d_{32} < L$ ), the drop is in the inertial subrange and the drop breakup is dominant by the inertial stress (Boxall et al. 2012) (Chen & Middleman 1967) (Rueger & Calabrese 2013a) (Sis et al. 2005; Coualoglou & Tavlarides 1977). In the viscous subrange, the Sauter mean diameter is smaller than the Kolmogorov length (Boxall et al. 2012) and drop breakup is determined by both inertial and viscous stress. It is also demonstrated that the breakup rate is defined by the maximum energy dissipation ( $\varepsilon_{max}$ ), and thus, it is reasonable to use  $\varepsilon_{max}$  for the calculation of  $\eta$  (Sajjadi et al. 2002) (Zhou & Kresta 1998a).

To define the range of drop size on the spectrum, Kolmogorov length and integral length was calculated for different geometries. Figure 15 shows a typical Kolmogorov length on the CLD spectrum.

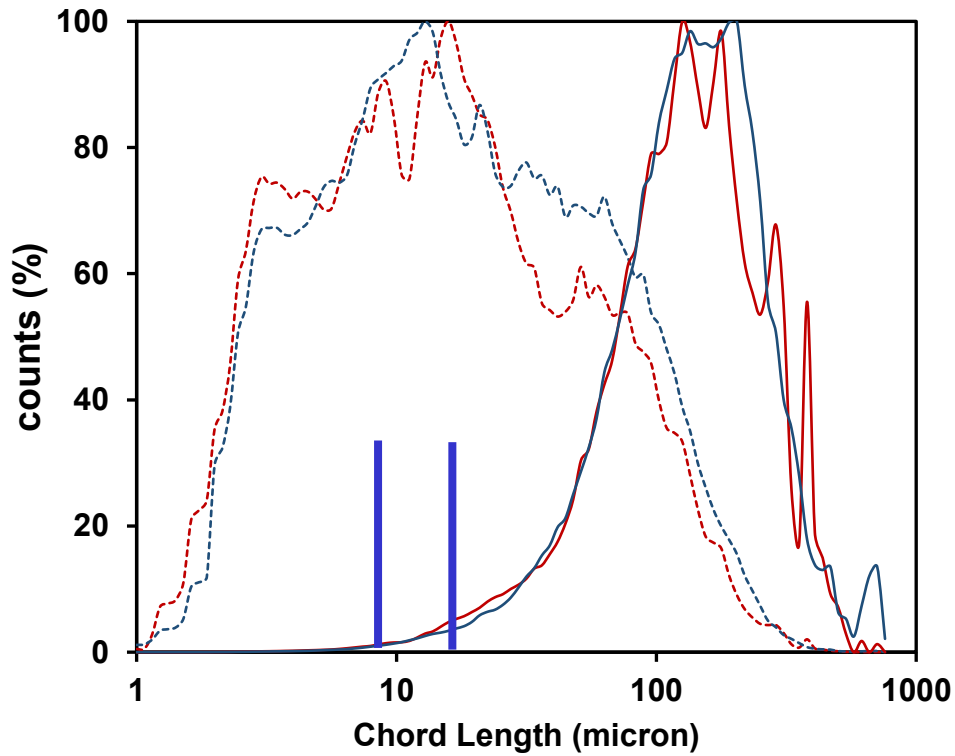


**Figure 15-Sample Kolmogorov length on the CLD spectrum**

The integral scale for the CIST and the ST was 3.8 mm and 12 mm, respectively. Comparison of the Kolmogorov length and Sauter mean chord length is summarized in Table 7. In all cases, the final chord length was much larger than the Kolmogorov microscale and much smaller than the turbulence macroscale. This indicates that the chord length was within the inertial subrange (Nishikawa et al. 1987; Becker et al. 2011). As the drop size is equal to or bigger than the chord length, the drop size was also within the inertial subrange.  $\eta$  was calculated for the geometries that the data for  $\varepsilon_{max}$  was available in the literature (Machado & Kresta 2013; Suzanne M. Kresta, Arthur W. Etchells, David S. Dickey 2015). Although  $cl_{32}$  was larger than  $\eta$ , comparison of number weighted chord length distribution with the corresponding  $\eta$  showed that considerable portion of

drop chord length (up to 40%) were smaller than the Kolmogorov length. Same result was reported by Zhou and Kresta (Zhou & Kresta 1998a). They observed more than 30% of drops smaller than the  $\eta$ . This is because Kolmogorov length scale is an estimate of the smallest drop size that can be broken by the eddies, but it does not predict the size of generated satellite drops, or drops formed by other processes such as tip streaming (Zhou & Kresta 1998a) (Rueger & Calabrese 2013a). More detailed work is required to determine the mechanisms which lead to the formation of these small sized drops.

**Table 7- Comparison of chord length and Kolmogorov scale**

<b>Setup</b>	$\frac{\epsilon_{max}}{\epsilon_{ave}}$	$\epsilon_{ave}$ (W/kg)	$\epsilon_{max}$ (W/kg)	$\eta$ ( $\mu\text{m}$ )	$cl_{32}$ ( $\mu\text{m}$ )
<b>ST-RT-10</b>	20.77	0.09	1.93	26.84	→ 140
<b>ST-RT-30</b>	20.77	0.18	3.72	22.76	→ 160
<b>ST-PBT-10</b>	18.46	0.13	2.40	25.41	→ 150
<b>ST-PBT-30</b>	18.46	0.25	4.53	21.68	→ 123
<b>ST-A310-10</b>	19.17	0.12	2.31	25.64	→ 146
<b>ST-A310-30</b>	19.17	0.14	2.71	24.64	→ 133
<b>CIST-RT-10</b>	8.28	1.92	15.9	15.8	→ 132
<b>CIST-RT-30</b>	8.28	0.3	2.5	25.2	→ 500
<b>CIST-A310-10</b>	17.38	3.4	59.4	11.4	→ 115
<b>CIST-A310-30</b>	17.38	6	104.3	9.9	→ 110

### 3.5 Scaling of Sauter Mean Chord Length

Previous correlations considered the scaling of the mean drop size with the drop Weber number (Hinze 1955; Maaß et al. 2012; Angle & Hamza 2006; Calabrese et al. 1986). These correlations only considered the effect of physical properties (viscosity, density, interfacial tension) and dispersed phase holdup, while the effect of geometry and operating parameters were ignored (Maaß et al. 2010). Moreover, the linear dependence of drop size on holdup and also, linear correlation of  $d_{32}$  and  $d_{max}$  are two main assumptions applied in these correlations that were not supported by experimental data (Kraume et al. 2004)(Angle & Hamza 2006) (Zhou & Kresta 1998a).

In this work, correlation of the Sauter mean chord length with the operating parameters such as power and mixing energy was explored. Chord length does not include any assumption for the shape of the drop and it can be reported for both spherical and non-spherical drops, thus correlations of chord length are applicable over wide range of systems. This is the first attempt reported so far to correlate the chord length with operating parameter.

#### *Scaling with power per mass*

Figure 16 shows the plot of Sauter mean chord length at the equilibrium ( $cl_{32-eq}$ ) versus power per mass (P/m). Two main point can be concluded from the graph.

First,  $cl_{32-eq}$ -P/m followed the same slope for all geometries, except for the 30% holdup in the CIST. This is because in the CIST-30, the top impeller was submerged into the oil phase, which resulted in a different drawdown dynamic caused by the local phase inversion happening in the CIST-30 that forms both water-in-oil (w/o) and oil-in-water (o/w) drops.

Second, the slope of the fitted line to the data (10% CIST, 10%,30% ST and IF) gave an exponent of -0.01. This indicates that power per mass has a little effect on the Sauter mean chord length and power per mass is not an appropriate scaling parameter.

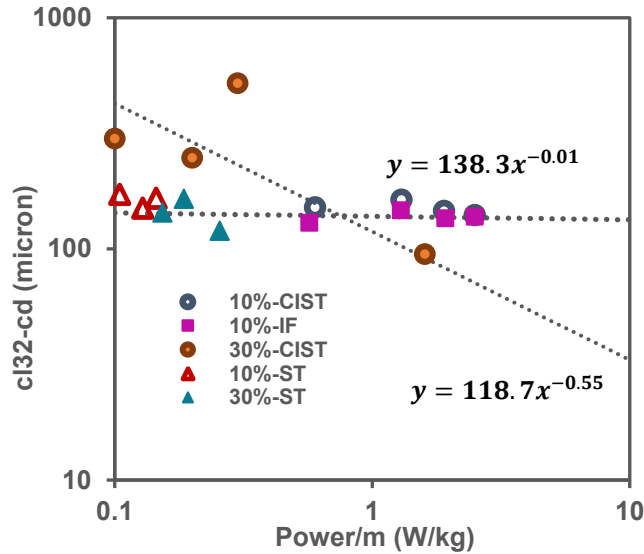


**Figure 16- Sauter mean chord length at the point of complete drawdown ( $cl_{32-cd}$ ) vs. Power per mass in log-log scale. 3 impellers (RT, PBT and A310) and two tank geometries (ST and CIST) were used. Configurations that the impeller is in the oil phase (CIST-30%) exhibit different slope than others**

### *Scaling with energy per mass*

The mixing energy per mass was calculated and the Sauter mean chord length versus energy at the complete drawdown time was plotted in Figure 17. As can be observed, Sauter mean chord length correlation with energy followed the same slope for 10% holdup in the CIST, 10% and 30% holdup in ST and impeller feed (-0.08), while the slope was different for the CIST-30 (-1.4), due to the different drawdown dynamic, as explained. In both cases,  $cl_{32-cd} - J_{cd}/m$  exhibited a clear trend, that

is, by increasing the  $J_{cd}$  the Sauter mean chord length decreased. Moreover, it can be concluded that the correlation of Sauter mean chord length with the mixing energy is independent of geometry and holdup when the impeller is in the continuous phase. In the case of the CIST-30% that the impeller was submerged in the oil phase, mixing energy and  $cl_{32-cd}$  were still correlated, but with different correlation.

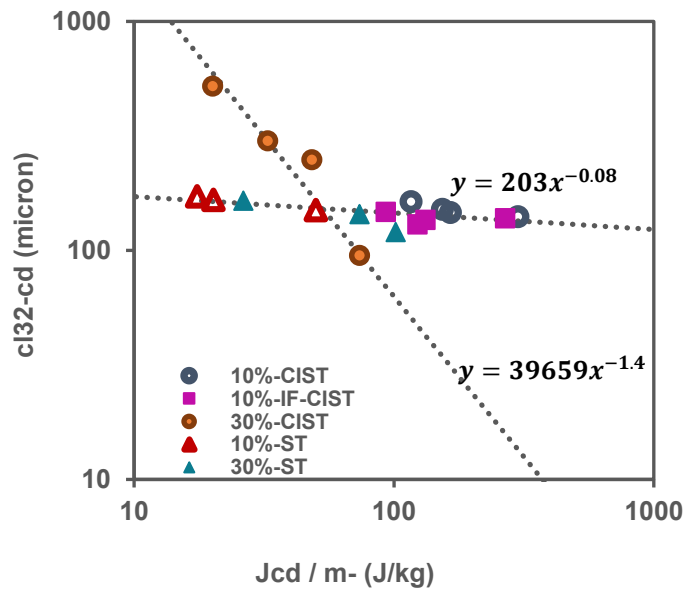


**Figure 17- Sauter mean chord length at the point of complete drawdown ( $cl_{32-cd}$ ) vs.  $J_{cd}/m$  in log-log scale. 3 impellers (RT, PBT and A310) and two tank geometries (ST and CIST) were used. Configurations that the impeller is in the oil phase (CIST-30%) exhibit different slope than others.**

Correlation of Sauter mean chord length and energy at equilibrium ( $cl_{32-eq}$  vs  $J_{eq}/m$ ) was also investigated. For  $cl_{32-eq}$  vs  $J_{eq}/m$  plot, the data was visibly scattered and there was no clear trend for chord length and equilibrium energy. This is partly because the  $J_{eq}$  was calculated from equilibrium time which was not a precise value.

*$J_{cd}$  scaling grouped by the impeller type*

Figure 18 shows the  $cl_{32}\text{-}J_{cd}/m$  at the point of complete drawdown grouped by the impeller type. The analysis leads to a similar conclusion as  $cl_{32\text{-}cd}$  vs  $J_{cd}/m$  that for all impeller configurations the Sauter mean chord length changes dramatically when one impeller is submerged in the dispersed phase. This result is in agreement with the literature on the effect of geometry on phase inversion during emulsion formation (Selkerl & Sleicher 1965)(Perazzo et al. 2015) (Yeo, et al 2000). These authors also reported the evidence for the phase inversion when the impeller was submerged in the second phase.

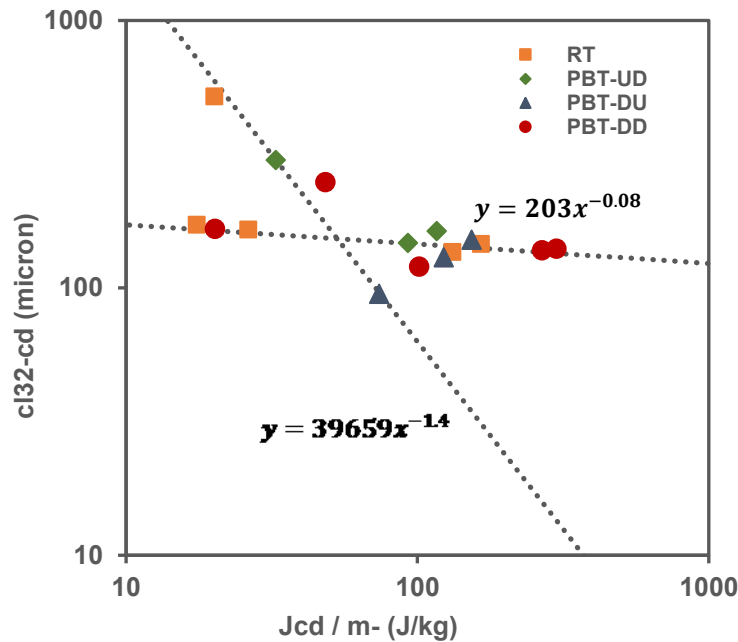


**Figure 18- Sauter mean chord length at the point of complete drawdown ( $cl_{32\text{-}eq}$ ) vs. complete drawdown energy grouped based on the impeller type. PBT-DD includes CIST-10, CIST-30, IF-10, ST-10 and ST-30. Fitted lines have similar slopes to Figure 16.**

The value of  $J_{cd}/m$ ,  $J_{eq}/m$  and  $P/m$  for surface layer and impeller feed experiments is summarized in Table 8.

From the data presented above, it can be concluded that at the point of complete drawdown, Sauter mean chord length scales well with the mixing energy per mass, in contrast to the power per mass, which showed no effect and  $J_{eq}/m$  that showed no clear trend.

**Table 8- Power consumed, equilibrium and complete drawdown energy per mass for Surface Layer and Impeller Feed experiments**

Impeller/Holdup	Surface Layer						Impeller Feed		
	CIST			ST			CIST		
	P/m (W/kg)	$J_{cd}/m$ (J/kg)	$J_{eq}/m$ (J/kg)	P/m (W/kg)	$J_{cd}/m$ (J/kg)	$J_{eq}/m$ (J/kg)	P/m (W/kg)	$J_{cd}/m$ (J/kg)	$J_{eq}/m$ (J/kg)
<b>RT-10</b>	1.92	165.3	2995.2	0.1	17.5	216	1.92	132.1	3340.8
<b>RT-30</b>	0.3	20.4	612	0.19	26.3	319.2	-	-	-
<b>PBT-DU-10</b>	0.57	153.7	1118	0.14	20.2	294	0.57	123.1	581.4
<b>PBT-UD-10</b>	1.29	116.5	2399.4				1.29	92.9	2167.2
<b>PBT-DD-10</b>	2.5	300	6000				2.5	267.8	2232
<b>PBT-DU-30</b>	1.6	75.2	2496	0.25	101.5	420	-	-	-
<b>PBT-UD-30</b>	0.12	33.3	259.2				-	-	-
<b>PBT-DD-30</b>	0.2	48.4	468				-	-	-
<b>A310-10</b>	3.42	N.A.	4924.8	0.13	50.1	273	3.42	3693.6	737.7
<b>A310-30</b>	6	N.A.	9000	0.15	73.8	270	-	-	-

## 4 Conclusion

Drawdown and dispersion of oil into water was studied. Number of different geometries were tested to examine the correlation of the complete dispersion speed ( $N_{cd}$ ) with the power per mass and mixing energy per mass ( $J_{cd}/m$ ). Results showed that the  $N_{cd}$  was not scalable with either power or energy.

The work was further extended by measuring the chord length distribution with the FBRM. The chord length distribution was broad and scattered at the beginning and gradually narrowed down as approaching the equilibrium time. After the equilibrium, distributions remained almost unchanged for the rest of the experiment. The FBRM measures chord length instead of the drop size. This seems physically meaningful when placed in the same frame as the spectrum of length scales in the turbulent flow.

Comparison of the Sauter mean chord length with the Kolmogorov length and integral length scale showed that the  $d_{32}$  was within the inertial subrange. However, considerable portion of number weighted chord length (up to 40%) were smaller than the Kolmogorov length, that may be attributed to the generation of the satellite drops during the breakup, or drops formed by processes such as tip streaming. More detailed work is required to determine the mechanisms which lead to the formation of these small sized drops.

At the point of complete dispersion, correlation of  $cl_{32}$  with power and energy was investigated. It was observed that  $cl_{32}-J_{cd}/m$  exhibited a clear trend. By increasing the  $J_{cd}$ , the chord length decreased. The  $cl_{32}$ -energy correlation was independent of geometry and holdup when the impeller was in the continuous phase. In the case of CIST-30% where the impeller was in the dispersed

phase,  $J_{cd}$  and  $cl_{32}$  were still correlated but the slope was different from other geometries. Despite energy, power showed no effect on  $cl_{32}$ .

## **5 Future Work**

This work can be extended in two areas of experimental and modelling. The experimental part works as the basis for the modelling section by providing required system data.

### **5.1 Extended Chord Length Measurement**

Current experimental work can be further extended to obtain more detailed data set to first study the liquid/liquid system experimentally with FBRM and secondly, to produce required data for the modelling of breakup and coalescence. Experiments can be further extended to both oil in water and water in oil. Moreover, it can be designed such that first dilute system where breakup is dominant be studied and then, more concentrated system with and without the surfactant be studied to study the both breakup and coalescence. The experimental design can be used to answer the following questions:

- Is it possible to generate reliable experimental data that is representative of the system and not biased by the lab or measurement condition?
- Does coalescence exist in the dilute system (e.g. 1%, 5%)?
- Is it possible to eliminate the coalescence completely in more concentrated system (e.g. 10%) by adding the surfactant?
- Are the results obtained for the oil-in-water system applicable for water-in-oil system?
- What is the difference between CIST and ST?

### **5.2 Breakup and Coalescence Modelling**

Although several studies have been performed to investigate the breakup/coalescence and define the equilibrium time, there are still some gaps. Most of the published studies are limited to the

breakup only. This is partly because coalescence is more complex. Coalescence is defined by both drop-drop interaction and drop-continues phase interaction, while breakup involves only drop-continues phase interaction (Chesters 1991). Moreover, brake up process can be studied independently from coalescence while that is not true for coalescence (Liao & Lucas 2010).

In most of the works, only very dilute system ( $\varphi < 2\%$ ) is considered (Becker et al. 2011; Gao, Li, Buffo, Podgorska, et al. 2016). In others that the system with the holdup as high as 40% is considered, the coalescence effect is neglected without further investigation (Maaß et al. 2012). Moreover, the combination of the effect of tank geometry, holdup, type of liquid and energy dissipation on the breakup in water in oil dispersion is not examined.

Current models published to predict the breakup have several limitations. All drop coalescence and breakup equations are developed based on the conservation equation and it is required that they accurately satisfy number, volume and mass conservation properties. However, some published models did not satisfy the conservation of mass (Solsvik et al. 2015). It is also reported by Solsvik that ignoring the effect of additives such as emulsifier in some models may results in under-prediction of breakup rate (Solsvik et al. 2015). However, this is not an issue in most of the works and becomes important when higher hold up (e.g.  $>30\%$ ) with high concentration of stabilizer is used.

Regarding the coalescence process, most of the work is dedicated to the development of new kernel and there are limited publications in terms of implementation of the model for the specific experimental system. In the work published by A. Bak and Podgorksa (Bak & Podgorska 2013), only system with very low concentration of dispersed phase ( $\varphi = 0.05\%$ ) is considered to study the coalescence. In the recent work published by D. Li (Li et al. 2017) only oil in water dispersion was

studied and the applicability of the obtained result for other types of dispersion (e.g. water in oil) was not examined.

Rueger and Calabrese (Rueger & Calabrese 2013a; Rueger & Calabrese 2013b) investigated the breakup in dilute water in oil dispersion ( $\phi = 0.001$ ) and then increased the holdup up to 50% to include the coalescence. Their work was limited to providing an equation for the transient drop size. Their work can be extended to define the breakup and coalescence process to provide better understanding of the system.

Regarding the experimental works, system properties and impurities could alter coalescence which makes the results very system dependent. The experiments must be performed with considerable caution to make sure the data is representative of a real system (e.g. extensive cleaning of the tank between experiments) (Paul et al. 2004).

In conclusion, combination of reliable experimental study with the careful numerical modelling of the breakup only system as well as system with both breakup and coalescence for both water-in-oil and oil-in water dispersion is crucial for the thorough understanding of liquid/liquid systems.

## References

- Abidin, M.I.I.Z., Raman, A.A.A. & Nor, M.I.M., 2013. Review on Measurement Techniques for Drop Size Distribution in a Stirred Vessel. *Industrial & Engineering Chemistry Research*, 52(46), pp.16085–16094.
- Afshar Ghotli, R. et al., 2013. Liquid-Liquid Mixing in Stirred Vessels: a Review. *Chemical Engineering Communications*, 200(5), pp.595–627.
- Alopaeus, V. et al., 2002. Simulation of the population balances for liquid–liquid systems in a nonideal stirred tank. Part 2—parameter fitting and the use of the multiblock model for dense dispersions. *Chemical Engineering Science*, 57(10), pp.1815–1825.
- Angle, C.W. & Hamza, H.A., 2006. Predicting the sizes of toluene-diluted heavy oil emulsions in turbulent flow Part 2: Hinze–Kolmogorov based model adapted for increased oil fractions and energy dissipation in a stirred tank. *Chemical Engineering Science*, 61(22), pp.7325–7335.
- Armenante, P.M., Huang, Y.-T. & Li, T., 1992. Determination of the minimum agitation speed to attain the just dispersed state in solid-liquid and liquid-liquid reactors provided with multiple impellers. *Chemical Engineering Science*, 47(9), pp.2865–2870.
- Armenante, P.M. & Huang, Y.T., 1992. Experimental determination of the minimum agitation speed for complete liquid-liquid dispersion in mechanically agitated vessels. *Industrial & Engineering Chemistry Research*, 31(5), pp.1398–1406.
- Azian, M.N. et al., 2001. Viscosity estimation of triacylglycerols and of some vegetable oils, based on their triacylglycerol composition. *Journal of the American Oil Chemists' Society*, 78(10), pp.1001–1005.
- Bak, A. & Podgórska, W., 2013. Drop breakage and coalescence in the toluene/water dispersions with dissolved surface active polymers PVA 88% and 98%. *Chemical Engineering Research and Design*, 91(11), pp.2142–2155.
- Bałdyga, J. et al., 2001. Effects of agitation and scale-up on drop size in turbulent dispersions: allowance for intermittency. *Chemical Engineering Science*, 56(11), pp.3377–3385.
- Baldyga, J. & Podgórska, W., 1998. Drop break-up in intermittent turbulence: Maximum stable and transient sizes of drops. *The Canadian Journal of Chemical Engineering*, 76(3), pp.456–470.
- Becker, P.J. et al., 2011. Investigation of discrete population balance models and breakage kernels for dilute emulsification systems. *Industrial and Engineering Chemistry Research*, 50(19), pp.11358–11374.
- Becker, P.J. et al., 2014. Monitoring silicone oil droplets during emulsification in stirred vessel: Effect of dispersed phase concentration and viscosity. *Canadian Journal of Chemical Engineering*, 92(2), pp.296–306.
- Bittorf, K.J. & Kresta, S.M., 2000. Active volume of mean circulation for stirred tanks agitated with axial impellers. *Chemical Engineering Science*, 55(7), pp.1325–1335.
- Bittorf, K.J. & Kresta, S.M., 2001. Three-dimensional wall jets: Axial flow in a stirred tank. *AIChE Journal*, 47(6), pp.1277–1284.
- Blount, J.M., 1995. *Mechanisms of drop breakage in dilute, agitated liquid–liquid systems*,. University of Maryland, College Park, MD.

- Boxall, J.A. et al., 2010. Measurement and calibration of droplet size distributions in water-in-Oil emulsions by particle video microscope and a focused beam reflectance method. *Industrial and Engineering Chemistry Research*, 49(3), pp.1412–1418.
- Boxall, J. a et al., 2012. Droplet size scaling of water-in-oil emulsions under turbulent flow. *Langmuir : the ACS journal of surfaces and colloids*, 28, pp.104–10.
- Calabrese, R. V, Wang, C.Y. & Bryner, N.P., 1986. Drop breakup in turbulent stirred-tank contactors. Part III: Correlations for mean size and drop size distribution. *AIChE Journal*, 32(4), pp.677–681.
- Cameirao, A. et al., 2012. Chord length distributions interpretation using a polydispersed population: Modeling and experiments. *Journal of Crystal Growth*, 342(1), pp.65–71.
- Ceylan, S., Kelbaliyev, G. & Ceylan, K., 2003. Estimation of the maximum stable drop sizes, coalescence frequencies and the size distributions in isotropic turbulent dispersions. *Colloids and Surfaces A: Physicochemical and Engineering Aspects*, 212(2–3), pp.285–295.
- Chapple, D. et al., 2002. The Effect of Impeller and Tank Geometry on Power Number for a Pitched Blade Turbine. *Chemical Engineering Research and Design*, 80(4), pp.364–372.
- Chatzi, E.G., Boutris, C.J. & Kiparissides, C., 1991. On-line monitoring of drop size distributions in agitated vessels. 1. Effects of temperature and impeller speed. *Industrial & Engineering Chemistry Research*, 30(3), pp.536–543.
- Chatzi, E.G., Boutris, C.J. & Kiparissides, C., 1991. On-Line Monitoring of Drop Size Distributions in Agitated Vessels. 1. Effects of Temperature and Impeller Speed. *Industrial & Engineering Chemistry Research*, 30(3), pp.536–543.
- Chen, H.T. & Middleman, S., 1967. Drop size distribution in agitated liquid-liquid systems. *AIChE Journal*, 13(5), pp.989–995.
- Cheng, D. et al., 2015. Experimental study on the dispersed phase macro-mixing in an immiscible liquid-liquid stirred reactor. *Chemical Engineering Science*, 126, pp.196–203.
- Chesters, A.K., 1991. The modelling of coalescence processes in fluid-liquid dispersions : a review of current understanding.
- Coulaloglou, C.A. & Tavlarides, L.L., 1977. Description of interaction processes in agitated liquid-liquid dispersions. *Chemical Engineering Science*, 32(11), pp.1289–1297.
- Delichatsios, M.A. & Probstein, R.F., 1976. The Effect of Coalescence on the Average Drop Size in Liquid-Liquid Dispersions. *Industrial & Engineering Chemistry Fundamentals*, 15(2), pp.134–138.
- Derksen, J.J. & Van Den Akker, H.E.A., 2007. Multi-Scale Simulations of Stirred Liquid-Liquid Dispersions. *Chemical Engineering Research and Design*, 85(5), pp.697–702.
- Deshpande, K.B. & Kumar, S., 2003. A new characteristic of liquid-liquid systems - Inversion holdup of intensely agitated dispersions. *Chemical Engineering Science*, 58(16), pp.3829–3835.
- Doulah, M.S., 1975. An Effect of Hold-up on Drop Sizes in Liquid-Liquid Dispersions. *Industrial & Engineering Chemistry Fundamentals*, 14(2), pp.137–138.
- Esch, D.D., D'ANGELO, P.J. & Pike, R.W., 1971. On minimum power requirements for emulsification of two-phase, liquid systems. *The Canadian Journal of Chemical Engineering*, 49(6), pp.872–875.
- Ferreira, L.S. & Trierweiler, J.O., 2009. Modeling and simulation of the polymeric nanocapsule formation process. *IFAC Proceedings Volumes (IFAC-PapersOnline)*, 7(PART 1), pp.405–410.

- Gao, Z., Li, D., Buffo, A., Podgórska, W., et al., 2016. Simulation of droplet breakage in turbulent liquid-liquid dispersions with CFD-PBM: Comparison of breakage kernels. *Chemical Engineering Science*, 142, pp.277–288.
- Gao, Z., Li, D., Buffo, A., Podgórska, W., et al., 2016. Simulation of droplet breakage in turbulent liquid-liquid dispersions with CFD-PBM: Comparison of breakage kernels. *Chemical Engineering Science*, 142, pp.277–288.
- Giapos, A., Pachatouridis, C. & Stamatoudis, M., 2005. Effect of the Number of Impeller Blades on the Drop Sizes in Agitated Dispersions. *Chemical Engineering Research and Design*, 83(12), pp.1425–1430.
- Heath, A.R. et al., 2002. Estimating average particle size by focused beam reflectance measurement (FBRM). *Particle and Particle Systems Characterization*, 19(2), pp.84–95.
- Hinze, J.O., 1955. Fundamentals of the hydrodynamic mechanism of splitting in dispersion processes. *AIChE Journal*, 1(3), pp.289–295.
- Hong, P.O. & Lee, J.M., 1985. Changes of the average drop sizes during the initial period of liquid-liquid dispersions in agitated vessels. *Industrial & Engineering Chemistry Process Design and Development*, 24(3), pp.868–872.
- Hong, P.O. & Lee, J.M., 1983a. Unsteady-state liquid-liquid dispersions in agitated vessels. *Industrial & Engineering Chemistry Process Design and Development*, 22(1), pp.130–135.
- Hong, P.O. & Lee, J.M., 1983b. Unsteady-state liquid-liquid dispersions in agitated vessels. *Industrial & Engineering Chemistry Process Design and Development*, 22(1), pp.130–135. Available at: <http://dx.doi.org/10.1021/i200020a021>. dy-state liquid-liq. *Industrial & Engineering Chemistry Process Design and Development*, 22(1), pp.130–135.
- Joshi, J.B. et al., 2011. CFD simulation of stirred tanks: Comparison of turbulence models. Part I: Radial flow impellers. *Canadian Journal of Chemical Engineering*, 89(1), pp.23–82.
- KATAOKA, T. & NISHIKI, T., 1986. DISPERSED MEAN DROP SIZES OF (W/0)/W EMULSIONS IN A STIRRED TANK. *Journal of Chemical Engineering of Japan*, 19(5), pp.408–412.
- Kato, S., Nakayama, E. & Kawasaki, J., 1991. Types of dispersion in agitated liquid-liquid systems. *The Canadian Journal of Chemical Engineering*, 69(1), pp.222–227.
- Khazam, O. & Kresta, S.M., 2008. Mechanisms of solids drawdown in stirred tanks. *The Canadian Journal of Chemical Engineering*, 86(4), pp.622–634.
- Kraume, M., 2012. on-Line Monitoring of Fluid Particle Size Distributions in Agitated Vessels Using Automated Image Analysis. , (September), pp.10–13.
- Kraume, M., Gäbler, A. & Schulze, K., 2004. Influence of physical properties on drop size distributions of stirred liquid-liquid dispersions. *Chemical Engineering and Technology*, 27(3), pp.330–334.
- Lang, W., Sokhansanj, S. & Sosulski, F.W., 1992. Modelling the temperature dependence of kinematic viscosity for refined canola oil. *Journal of the American Oil Chemists' Society*, 69(10), pp.1054–1055.
- Laurenzi, F. et al., 2009. Experimental and computational analysis of immiscible liquid-liquid dispersions in stirred vessels. *Chemical Engineering Research and Design*, 87(4), pp.507–514.
- Leng, D.E. & Calabrese, R. V, 2004. Immiscible Liquid–Liquid Systems. In *Handbook of Industrial*

- Mixing*. John Wiley & Sons, Inc., pp. 639–753.
- Li, D. et al., 2017. Droplet breakage and coalescence in liquid–liquid dispersions: Comparison of different kernels with EQMOM and QMOM. *AIChE Journal*, 63(6), pp.2293–2311.
- Liao, Y. & Lucas, D., 2009. A literature review of theoretical models for drop and bubble breakup in turbulent dispersions. *Chemical Engineering Science*, 64(15), pp.3389–3406.
- Liao, Y. & Lucas, D., 2010. A literature review on mechanisms and models for the coalescence process of fluid particles. *Chemical Engineering Science*, 65(10), pp.2851–2864.
- Maaß, S. et al., 2007. Experimental Investigations and Modelling of Breakage Phenomena in Stirred Liquid/Liquid Systems. *Chemical Engineering Research and Design*, 85(5), pp.703–709.
- Maaß, S. et al., 2010. Prediction of drop sizes for liquid–liquid systems in stirred slim reactors—Part I: Single stage impellers. *Chemical Engineering Journal*, 162(2), pp.792–801.
- Maaß, S., Grunig, J. & Kraume, M., 2009. Measurement Techniques for Drop Size Distributions in Stirred Liquid – Liquid Systems. *Chemical and Process Engineering*, 30, pp.635–651.
- Maaß, S., Paul, N. & Kraume, M., 2012. Influence of the dispersed phase fraction on experimental and predicted drop size distributions in breakage dominated stirred systems. *Chemical Engineering Science*, 76, pp.140–153.
- Machado, M.B. et al., 2013. Transition from turbulent to transitional flow in the top half of a stirred tank. *Chemical Engineering Science*, 98, pp.218–230.
- Machado, M.B. & Kresta, S.M., 2013. The confined impeller stirred tank (CIST): A bench scale testing device for specification of local mixing conditions required in large scale vessels. *Chemical Engineering Research and Design*, 91(11), pp.2209–2224.
- Mostafavi, M., Petersen, S. & Ulrich, J., 2016. The influence of air bubbles on the measurement of different crystal sizes and suspension densities by the 3D ORM measurement technique. , (February), pp.1–6.
- Nieves-Remacha, M.J., Kulkarni, A.A. & Jensen, K.F., 2012. Hydrodynamics of Liquid–Liquid Dispersion in an Advanced-Flow Reactor. *Industrial & Engineering Chemistry Research*, 51(50), pp.16251–16262.
- Nishikawa, M., Mori, F. & Fujieda, S., 1987. Average Drop Size in a Liquid-Liquid Phase Mixing Vessel. *Journal of Chemical Engineering of Japan*, 20(1), pp.82–88.
- Padron, G.A., 2005. *Effect of surfactants on drop size distribution in a batch, rotor–stator mixer*. University of Maryland, MD, USA.
- Pandey, A., Smith, B. & Redman, T., 2013. Best Practice for Separations in Mining and Oil Sands Operations A Review of Modern Technologies.
- Paul, E.L., Atiemo-Obeng, V.A. & Kresta, S.M., 2004. *Handbook of industrial mixing : science and practice*, Wiley-Interscience.
- Perazzo, A., Preziosi, V. & Guido, S., 2015. Phase inversion emulsification: Current understanding and applications. *Advances in Colloid and Interface Science*, 222, pp.581–599.
- Poblete, I.B., Castor, C.A. & Nele, M., 2016. On-Line Monitoring of Chord Distributions in Liquid – Liquid Dispersions and Suspension Polymerizations by Using the Focused Beam Reflectance Measurement Technique. , (Cld).

- Podgórska, W. & Marchisio, D.L., 2016. Modeling of turbulent drop coalescence in the presence of electrostatic forces. *Chemical Engineering Research and Design*, 108(1977), pp.30–41.
- Quinn, J.A. & Sigloh, D.B., 1963. Phase inversion in the mixing of immiscible liquids. *The Canadian Journal of Chemical Engineering*, 41(1), pp.15–18.
- Razzaghi, K. & Shahraki, F., 2010. On the effect of phase fraction on drop size distribution of liquid–liquid dispersions in agitated vessels. *Chemical Engineering Research and Design*, 88(7), pp.803–808.
- Rueger, P.E. & Calabrese, R. V., 2013a. Dispersion of water into oil in a rotor-stator mixer. Part 1: Drop breakup in dilute systems. *Chemical Engineering Research and Design*, 91(11), pp.2122–2133.
- Rueger, P.E. & Calabrese, R. V., 2013b. Dispersion of water into oil in a rotor-stator mixer. Part 2: Effect of phase fraction. *Chemical Engineering Research and Design*, 91(11), pp.2134–2141.
- Ruf, A., Worlitschek, J. & Mazzotti, M., 2000. Modeling and experimental analysis of PSD measurements through FBRM. *Particle and Particle Systems Characterization*, 17(4), pp.167–179.
- Salager, S.E. et al., 2001. Influence of the Stirrer Initial Position on Emulsion Morphology. Making Use of the Local Water-to-Oil Ratio Concept for Formulation Engineering Purpose. *Industrial & Engineering Chemistry Research*, 40(22), pp.4808–4814.
- Schümann, H. et al., 2015. Droplet Size Measurements in Oil–Water Dispersions: A Comparison Study Using FBRM and PVM. *Journal of Dispersion Science and Technology*, 36(10), pp.1432–1443.
- Selkerl, A.H. & Sleicher, C.A., 1965. Factors Affecting which Phase will Disperse when Immiscible Liquids are Stirred Together. , pp.298–301.
- Sis, H., Kelbaliyev, G. & Chander, S., 2005. Kinetics of drop breakage in stirred vessels under turbulent conditions. *Journal of Dispersion Science and Technology*, 26(5), pp.565–573.
- Skelland, A.H.P. & Lee, J.M., 1978. Agitator speeds in baffled vessels for uniform liquid-liquid dispersions. *Industrial & Engineering Chemistry Process Design and Development*, 17(4), pp.473–478.
- Skelland, A.H.P. & Ramsay, G.G., 1987. Minimum agitator speeds for complete liquid-liquid dispersion. *Industrial & Engineering Chemistry Research*, 26(1), pp.77–81.
- Skelland, A.H.P. & Seksaria, R., 1978. Minimum Impeller Speeds for Liquid-Liquid Dispersion in Baffled Vessels. *Industrial & Engineering Chemistry Process Design and Development*, 17(1), pp.56–61
- Solsvik, J. et al., 2015. Viscous Drop Breakage in Liquid-Liquid Stirred Dispersions: Population Balance Modeling. *Journal of Dispersion Science and Technology*, 36(4), pp.577–594.
- Soos, M. et al., 2013. Determination of maximum turbulent energy dissipation rate generated by a rushton impeller through large eddy simulation. *AIChE Journal*, 59(10), pp.3642–3658.
- Sprow, F.B., 1967. Distribution of drop sizes produced in turbulent liquid–liquid dispersion. *Chemical*
- Suzanne M. Kresta, Arthur W. Etchells, David S. Dickey, V.A.A.-O., 2015. *Advances in industrial mixing : a companion to the Handbook of industrial mixing*, Wiley.
- Treybal, R.E., 1958. Estimation of the stage efficiency of simple, agitated vessels used in mixer-settler extractors. *AIChE Journal*, 4(2), pp.202–207.

- Vankova, N. et al., 2007. Emulsification in turbulent flow. 1. Mean and maximum drop diameters in inertial and viscous regimes. *Journal of Colloid and Interface Science*, 312(2), pp.363–380.
- Wang, C.Y. & Calabrese, R. V, 1986. Drop Breakup in Turbulent Stirred-Tank Reactors .2. Relative Influence of Viscosity and Interfacial-Tension. *Aiche Journal*, 32(4), pp.667–676.
- Wang, T. et al., 2013. Numerical simulation of a pitched-blade turbine stirred tank with mirror fluid method. *Canadian Journal of Chemical Engineering*, 91(5), pp.902–914.
- Wang, W. et al., 2013. Evolution of dispersed drops during the mixing of mineral oil and water phases in a stirring tank. *Chemical Engineering Science*, 91, pp.173–179.
- Yeo, L.Y.; Matar, O.K.; Perez de Ortiz, E.S.; Hewitt, G., 2000. Phase Inversion and Associated Phenomena. *Multiphase Sci. Technol*, 12(51), p.116.
- Yeo, L.Y. et al., 2002. Shorter communication A simple predictive tool for modelling phase inversion in liquid – liquid dispersions. *Chemical Engineering*, 57, pp.1069–1072.
- You, S.T. et al., 2014. Multiple-impeller stirred vessel studies. *Reviews in Chemical Engineering*, 30(3), pp.323–336.
- Zhou, G. & Kresta, S.M., 1998a. Correlation of mean drop size and minimum drop size with the turbulence energy dissipation and the flow in an agitated tank. *Chemical Engineering Science*, 53(11), pp.2063–2079.
- Zhou, G. & Kresta, S.M., 1998b. Evolution of drop size distribution in liquid-liquid dispersions for various impellers. *Chemical Engineering Science*, 53(11), pp.2099–2113.
- Zhou, G. & Kresta, S.M., 1996. Impact of tank geometry on the maximum turbulence energy dissipation rate for impellers. *AIChE Journal*, 42(9), pp.2476–2490.

## **Appendix A: Conversion of Chord Length Distribution to Drop Size Distribution**

### **Review of Available Methods**

Several authors have published empirical or theoretical approaches for conversion of chord length distribution. Most of these approaches are based on the argument that drop size distribution can be well represented by a log-normal distribution, which is supported by the several experimental results (Hu et al., 2006).

Weimer et al. (1985) suggested one of the earliest conversion methods. In this model, spherical drops are assumed and using the Pythagorean theorem the mean drop size is calculated from mean chord length. Clark and Turton (1988) reported a second method which assumes a functional size-independent shape for the drops and the probability density function of drop size. The chord length is then related to drop size. This method suffers from the stability problems of inverse matrix calculations.

The probability apportioning method (PAM) is a second class of methods. These methods assume that the drop diameter bins are known and back-calculates the diameter distribution from the chord length distribution. Since the drop diameter distribution is not known, a trial set of diameter bins has to be chosen. Problems arise in the solution when there is insufficient chord length data in narrow bins. Also, in the probability apportioning method each set of data is used in isolation from the others and does not benefit from the collective information. This method works satisfactorily only when the diameter ranges are known (Langston et al., 2001; Simmons et al., 1999).

Experimental studies suggest that none of the techniques above satisfactorily transform a chord length distribution to the drop size distribution.

To overcome the problems of previously published methods, an algorithm was proposed by Ruf et al. (2000) assuming that the drop velocity relative to the probe is negligible and all drop have the same shape. The results of this model are sensitive to the number of groups that the drop diameter data are divided into and the “noise” in the population of the largest size. If the number of groups is increased beyond some value, the backward transform becomes unstable, yielding irregular and sometimes negative values.

Another attempt was report by Hu et al. (2006). In this model they assumed that the measurement is always biased towards larger drops (which is not always the case for FBRM). It tried to remove the problem of noisy/ negative drop size distribution by adding smoothing equations in the backward conversion. The main drawback of this model is that the fixed geometrical equation is assumed to relate the chord length to the drop size, which may not be accurate depending on the position of drop relative to the probe.

Among all reviewed methods, the model proposed by Hukkanen and Braatz (2003) seemed most promising. This model is based on the algorithm proposed by Ruf et al. (2000) with modifications applied, which result in a stable model. The model was tested for a known drop size distribution. First, the chord length distribution was measured as if by random intersections through the drop using FBRM, and then the drop size distribution was calculated from an inverse matrix transformation. The calculated drop size distribution and original drop size distribution showed good agreement.

### Method proposed by Hukkanen and Braatz (2003)

The measured chord lengths are collected in  $n$  bins and form a matrix  $C$ , where  $c(D_j, D_{j+1})$  is the chord number distribution of a bin of  $D_j \leq D < D_{j+1}$ . The drop size distribution is represented by  $f$ , where each element represents the number of drops within the range.

$$c = \begin{pmatrix} c(D_1, D_2) \\ \vdots \\ c(D_n, D_{n+1}) \end{pmatrix} \quad f = \begin{pmatrix} f(D_1, D_2) \\ \vdots \\ f(D_n, D_{n+1}) \end{pmatrix}$$

The chord length distribution is related to the drop size through probability functions,  $P$  which is calculated for each.

$$C = Pf$$

$P$  is calculated from the following equation:

$$P_i(\hat{D}_j) = \begin{cases} \sqrt{1 - \left(\frac{D_i}{\hat{D}_j}\right)^2} - \sqrt{1 - \left(\frac{D_{i+1}}{\hat{D}_j}\right)^2} & i < j \\ \sqrt{1 - \left(\frac{D_i}{\hat{D}_j}\right)^2} & i = j \\ 0 & i > j \end{cases}$$

Where:

$$\hat{D}_j \in [D_j, D_{j+1})$$

And  $\widehat{D}_j$  is the characteristic size of each bin. To define the  $\widehat{D}_j$  some assumption must be made on how drops are distributed within each bin. One reasonably accurate approach is to assume “Midpoint” distribution of the drops in the bin. The characteristic size is defined as:

$$\hat{D}_j = \frac{1}{2}(D_j + D_{j+1})$$

By replacing it, P becomes:

$$P_{ij} = \begin{cases} \sqrt{1 - \left(\frac{2D_i}{D_j + D_{j+1}}\right)^2} - \sqrt{1 - \left(\frac{2D_{i+1}}{D_j + D_{j+1}}\right)^2} & i < j \\ \sqrt{1 - \left(\frac{2D_i}{D_j + D_{j+1}}\right)^2} & i = j \\ 0 & i > j \end{cases}$$

Using focused beam reflectance measurement, we measure matrix C. The matrix P can be calculated based on the information on the bin sizes. Then, the inverse transformation must be applied to calculate the matrix f, which is drop size distribution.

$$f = P^{-1}c$$

Sometimes, computation of the drop size distribution by direct matrix inversion can generate nonphysical or negative values due to measurement errors and poor matrix conditioning. This issue is avoided by introducing a “smoothing” parameter and ridge regression to replace the original inverse equation by the following equation:

$$f = (\gamma I + P^T P)^{-1} P^T c$$

$\gamma$  is an arbitrary value between 0 and 1 and is selected so that the calculated drop size distribution is smooth. The estimated drop size distribution can be reported as a number distribution, volume distribution or cumulative form of either of these two distributions, as required.

### **Coding and Numerical Results**

The conversion algorithm proposed by Hukkanen and Braatz (2003) was selected for its numerical stability and accuracy. Two sets of codes were developed using Matlab. In one set, a log-normal distribution function is assumed for the drop size distribution. Using that function, a simulated chord length distribution is calculated. In the next step, the simulated chord length distribution is used to compute the drop size distribution. The original and calculated drop size distribution are compared below to assess the accuracy of the model. Figure presents the original vs. calculated drop size distribution. It can be observed that the shape of calculated and initial drop size distribution is similar, confirming that the method predicted the overall feature of drop size distribution correctly (i.e. the scale (shape) and location (modal class) of the log-normal distribution).

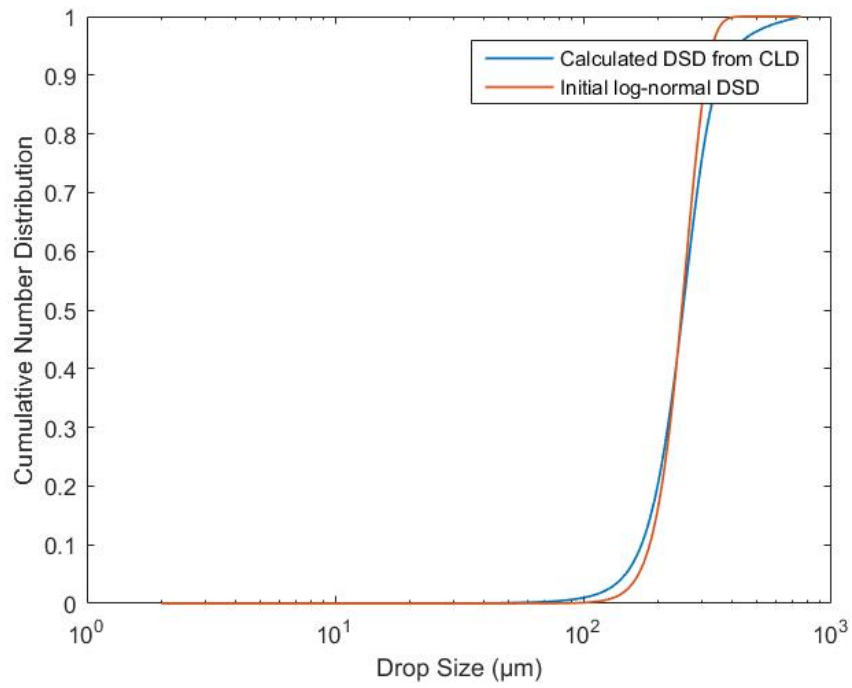
In the second Matlab code, an arbitrary experimental chord length distribution is generated. Using matrix inversion and ridge regression, the number drop size distribution is estimated from the known chord length distribution. The volume distribution drop size distribution and cumulative drop size distributions are then calculated.

Figure A-2-Experimental Chord Length Distribution measured by FBRM

, Figure A-3-Drop size distribution calculated from experimental chord length distribution using direct matrix inversion

A-3 and Figure A-4-Cumulative drop volume distribution computed from experimental chord length distribution

A-4 show experimental chord length distribution, calculated drop number distribution and cumulative drop volume distribution, respectively.



**Figure A-1-Cumulative log-normal drop size distribution vs. Calculated drop size distribution from matrix inversion**

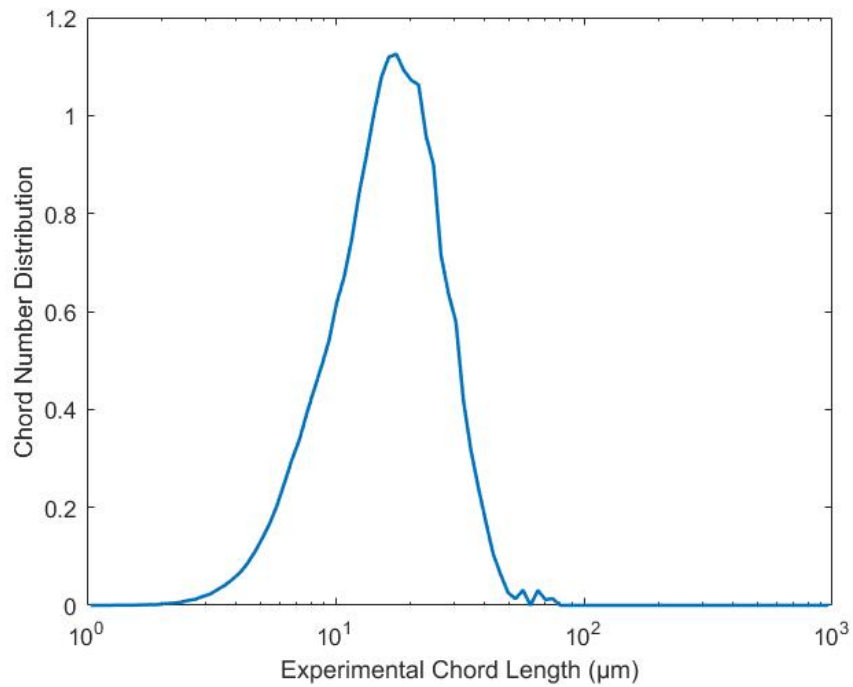


**Figure A-2-Experimental Chord Length Distribution measured by FBRM**

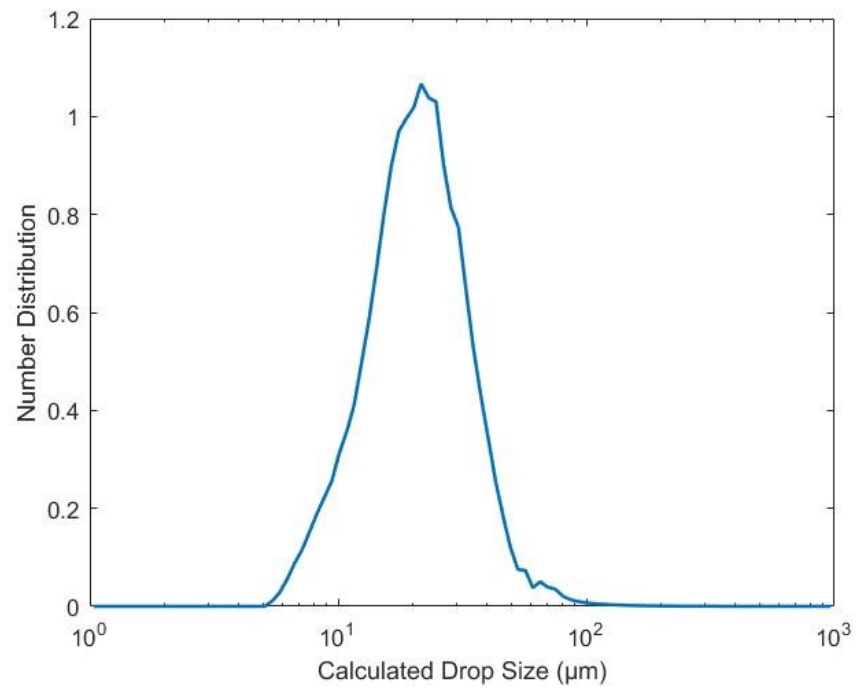


**Figure A-3-Drop size distribution calculated from experimental chord length distribution using direct matrix inversion**

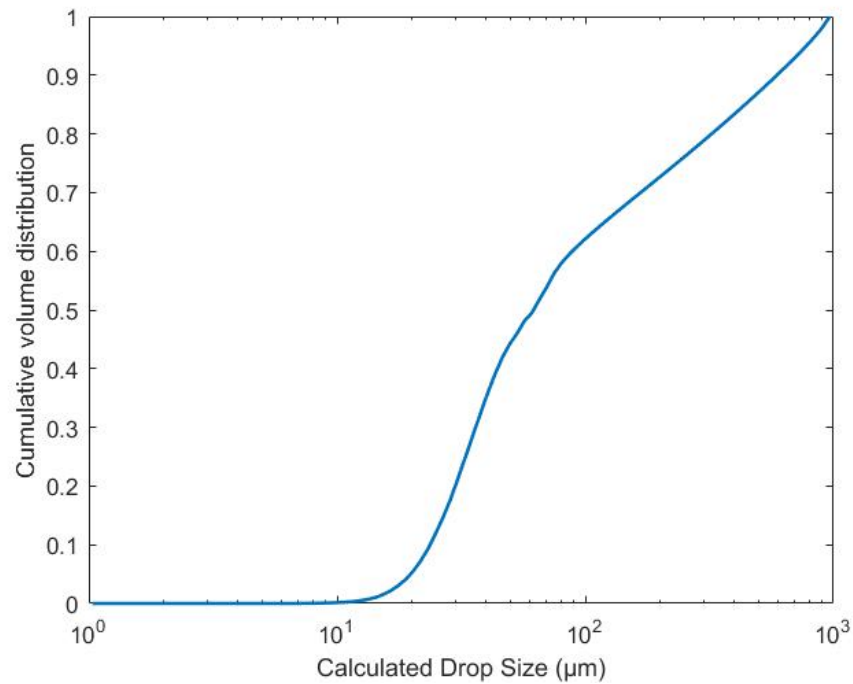


**Figure A-4-Cumulative drop volume distribution computed from experimental chord length distribution**

Midpoint

```
function P = MidPoint(CB)

n = size(CB,1);
P = zeros(n-1,n-1);

for j=2:(n-1)
    for i=1:(j-1)
        P(i,j) = sqrt(1-(2*CB(i)/(CB(j)+CB(j+1)))^2) - sqrt(1-(2*CB(i+1)/(CB(j)+CB(j+1)))^2);
    end
end

for j=1:(n-1)
    P(j,j) = sqrt(1-(2*CB(j)/(CB(j)+CB(j+1)))^2);
end

end
```

Normalized\_Var

```
function normalized = normalize_var(DSD, 0, 1)

% Normalize to [0, 1]:
m = min(DSD);
```

```

range = max(DSD) - m;
DSD_Norm = (DSD - m) / range;

FBRM_data= xlsread('FBRMdata');% Original excel file generated by FBRM
FBRM_data(:,1:4)=[]; % To remove unwanted columns from original input file
nn=size(FBRM_data,1);
BB=FBRM_data';
CB= BB(:,2);% Channel band defined by FBRM software, the midpoint data which
is representative CLD in each bin is defined from channel band
(CLDi=0.5*(CBi+CBi+1))

mm=size(FBRM_data',1);
ss=mm-1;
CC=FBRM_data(:,1:ss);
CC=CC';
CLD=CC(:,5:nn); % # of particles corresponding each Chord length

% Calculate the chord from CB using midpoint equation
m = size(CB,1);
for i=1:m-1
    C(i)=(CB(i)+CB(i+1))/2;
end

% To calculate the drop size from this formula: DSD = ((gama*I + PT*P)-
1)*PT*CLD

Gama=0.2; % correction factor used in equation 14 of reference paper
P=MidPoint(CB); % Probability density function defined by mid point
assumption
PT=transpose(P); % Transpose of matrix P
a=size(PT);
n = size(CB,1);

I=eye(n-1,n-1); % Identity matrix
sizeeye=size(I);
PTP=PT*P;
c=size(PTP);
INV=inv(Gama*I+PTP); % Inverse matrix used in eq.14 to calculate the DSD

% As the input data includes more than one DSD (different time-lapse)loop %
function should be used to calculate the DSD
input=size(CLD',1);

for i=1:input

    DSD(:,i)=INV*PT*CLD(:,i); % Calculated Drop size distribution based on
the experimental CLD using matrix inversion
end

% to remove negative values from DSD

a=size(DSD,1);
b=size(DSD',1);

for i=1:a
    for j=1:b

```

```

    if DSD(i,j)<0
        DSD_modified(i,j)=0;
    else
        DSD_modified(i,j)=DSD(i,j);
    end
end
end

% To calculate the volume distribution DSD from non-zero DSD

    for i=1:a
        for j=1:b

            DSD_vol(i,j)=DSD_modified(i,j)*(pi*(C(i)^3)/6);

        end
    end

%To calculate the cumulative volume distribution
for i=1:input

    V(i)=sum(DSD_vol(:,i)); % sum of all volume DSDs in each column
    CUMVDSD(:,i)=cumsum(DSD_vol(:,i))/V(i); % It calculates the cumulative
drop size distribution for each chord length data
end

% d32= (sigma (nidi^3))/(sigma (nidi^2))
% m is the number of size classes describing the DSD, ni the number of drops,
% and di the nominal diameter of drops in size class i.

% To calculate the Sauter mean diameter
    for i=1:a
        for j=1:b

            A(i,j)=DSD_modified(i,j)*(C(i)^3);
            B(i,j)=DSD_modified(i,j)*(C(i)^2);

        end
    end

    for i=1:input

        S1(i)=sum(A(:,i));
        S2(i)=sum(B(:,i));
        Sauter(i)=S1(i)/S2(i); % Sauter= sauter mean DSD

    end

% To calculate Square weighted DSD (yi= niDSD^2/sigma(niDSDi^2)

for i=1:a
    for j=1:b

```

```

    SQ1(i,j)=DSD_modified(i,j)*(C(i)^2);

end
end

for i=1:input

    sigma1(i)=sum(SQ1(:,i));
    Sq_DSD(:,i)=(SQ1(:,i))/sigma1(i); % sq_DSD= Square weighted DSD
end

% To calculate Cubic weighted DSD (yi= niDSD^3/sigma(niDSDi^3))

for i=1:a
    for j=1:b

        VOL1(i,j)=DSD_modified(i,j)*(C(i)^3);

    end
end

for i=1:input

    sigma3(i)=sum(VOL1(:,i));
    Cub_DSD(:,i)=(VOL1(:,i))/sigma3(i); % VOL_DSD= Cubic weighted DSD
end

% To calculate Volume average DSD (dm=(sigma(viDSDi)/(6/pi))^(1/3))

for i=1:a
    for j=1:b

        vol_ave(i,j)=DSD(i,j)*( pi*(C(i)^3)/6);

    end
end

for i=1:input

    dm(i)=(sum(vol_ave(:,i))/(6/pi))^(1/3);

end

% To calculate Square weighted CLD (yi= niCLD^2/sigma(niCLDi^2))

for i=1:a
    for j=1:b

        SQ2(i,j)=CLD(i,j)*(C(i)^2);

    end
end

for i=1:input

    sigma2(i)=sum(SQ2(:,i));

```

```

    Sq_CLD(:,i)=(SQ2(:,i))/sigma2(i); % sq_CLD= Square weighted CLD
end

% To calculate Cubic weighted CLD (yi= niCLD^3/sigma(niCLDi^3)

    for i=1:a
        for j=1:b

            VOL2(i,j)=CLD(i,j)*(C(i)^3);

        end
    end

    for i=1:input

        sigma4(i)=sum(VOL2(:,i));
        Cub_CLD(:,i)=(VOL2(:,i))/sigma4(i);
    end

% To Add a corresponding time to calculated DSD, assuming time interval of 10
sec
Timepoint=size(DSD_modified',1);
T=zeros(Timepoint,1)';

for i=2:Timepoint
    Time_interval=10;
    T(i)=T(i-1)+Time_interval;
end

DSD_Time=[T;DSD_modified];
CUMVDSD_Time=[T;CUMVDSD];

% To export the Number DSD and cumulative volume DSD to Excel file
xlswrite('Modified number DSD.xlsx', DSD_Time, 'Sheet1' , 'A1');
xlswrite('Cumulative volume DSD.xlsx', CUMVDSD_Time, 'Sheet1' , 'A1');

% To plot the chord density, Number DSD and cumulative volume DSD

semilogx(C,CLD(:,110) , 'LineWidth',1.5)
xlabel('Experimental Chord Length (µm)')
ylabel('Chord Number Distribution')

figure

semilogx(C,DSD_modified(:,110) , 'LineWidth',1.5)
xlabel('Calculated Drop Size (µm)')
ylabel('Number Distribution')

figure

semilogx(C,CUMVDSD(:,110) , 'LineWidth',1.5)
xlabel('Calculated Drop Size (µm)')
ylabel('Cumulative Volume Distribution')

```

```

figure

plot(T,Sauter,'LineWidth',1.5)
xlabel('Time (Sec)')

hold

plot(T,dm,'LineWidth',1.5)
legend('Sauter Mean Diameter ( $\mu\text{m}$ )','Volume Average Diameter ( $\mu\text{m}$ )')

%-----
%-----
%-----
%-----

% This part includes extra info and calculation, which is not required for
% this step of project.

% To Normalize the calculated Number DSD
for i=1:input
    N(i)=sum(DSD_modified(:,i)); % sum of all DSDs
    DSD_Norm(:,i) = (DSD_modified(:,i) - min(DSD_modified(:,i))) / (N(i)-
min(DSD_modified(:,i)));
end

% To calculate the cumulative number distribution
for i=1:input
    N(i)=sum(DSD_modified(:,i));
    CUMDSD(:,i)=cumsum(DSD(:,i)/N(i));

end

% To Normalize the calculated volume DSD
for i=1:input
    V(i)=sum(DSD_vol(:,i));
    DSD_Norm_vol(:,i) = (DSD_vol(:,i) - min(DSD_vol(:,i))) / (V(i)-
min(DSD_vol(:,i)));

end

```

## Appendix B: SOP and Experimental Procedure

### Main Hazards:

- Spill and slip hazard
- Hot floodlight (used for  $N_{id}$  and  $N_{cd}$  measurements)
- Hot motor (used to rotate the shaft)
- Falling off the ladder (when plug in/out the cords)

### Experimental procedure:

1. Prepare impellers: put impellers of desired type onto the shaft at specified heights
2. Prepare CIST and ST: insert bottom plate and baffles into CIST and impeller shaft
3. Prepare CIST lid by inserting shaft with impellers
4. The experiments are performed for 30% and 10% of canola oil and water in ST as well as CIST
5. Before starting the experiment, the impeller shaft is attached to the motor and is setup in the CIST and ST tanks as per the specifications mentioned in Table 1.
6. Fill up the tank with the required amount of water.
7. Add two to three drops of red colored Leak-Detecting Dye by Bright Dyes Solvent, Kingscote Chemicals Inc (only for  $N_{id}$  and  $N_{cd}$  measurements)
8. Clean FBRM probe with the continuous phase liquid until counts are below 300
9. Immerse probe in oil for calibration with dispersed phase
10. Insert the FBRM probe into the tank until tip is halfway between shaft and wall
11. Make sure probe is in  $45^\circ$  with the main flow direction
12. Pour the canola oil slowly into the tank in order to avoid mixing of the immiscible liquids.
13. Set motor at  $N_{cd}$  and turn on the motor
14. Start FBRM software and create new file.
15. Start recording on FBRM.
16. Once the FBRM and tank are set up, the motor is turned on and the torque at  $N_{cd}$  is recorded.
17. In order to determine  $t_{cd}$ , adjust the impeller speed to  $N_{cd}$ . Start the motor and record  $t_{cd}$  for oil in water at  $N_{cd}$
18. When CLD is measured for long enough time, clean probe and empty/wash the vessel